

# A neuronal architecture underlying autonomic dysreflexia

<https://doi.org/10.1038/s41586-025-09487-w>

Received: 6 May 2024

Accepted: 1 August 2025

Published online: 17 September 2025

Open access

 Check for updates

Jan Elaine Soriano<sup>1,2,3,4,5,14</sup>, Remi Hudelle<sup>4,5,14</sup>, Lois Mahe<sup>4,5,6</sup>, Matthieu Gautier<sup>4,5,6</sup>, Alan Yue Yang Teo<sup>4,5</sup>, Michael A. Skinnider<sup>7</sup>, Achilleas Laskaratos<sup>4,5</sup>, Steven Ceto<sup>4,5</sup>, Claudia Kathe<sup>4,5,8</sup>, Thomas Hutson<sup>9</sup>, Rebecca Charbonneau<sup>1</sup>, Fady Grgis<sup>1</sup>, Steve Casha<sup>1</sup>, Julien Rimok<sup>1,2,3,10</sup>, Marcus Tso<sup>1,2,3,10</sup>, Kelly Larkin-Kaiser<sup>1,2,3,10</sup>, Nicolas Hankov<sup>4,5</sup>, Aasta Gandhi<sup>4,5</sup>, Suje Amir<sup>4,5</sup>, Xiaoyang Kang<sup>11</sup>, Yashwanth Vyza<sup>5,12</sup>, Eduardo Martin-Moraud<sup>4,5</sup>, Stephanie Lacour<sup>5,12</sup>, Robin Demesmaeker<sup>4,5</sup>, Leonie Asboth<sup>4,5</sup>, Quentin Barraud<sup>4,5</sup>, Mark A. Anderson<sup>4,5,8</sup>, Jocelyne Bloch<sup>4,5,6,13</sup>, Jordan W. Squair<sup>4,5,6,13,15</sup>✉, Aaron A. Phillips<sup>1,2,3,10,15</sup>✉ & Gregoire Courtine<sup>4,5,6,13,15</sup>✉

Autonomic dysreflexia is a life-threatening medical condition characterized by episodes of uncontrolled hypertension that occur in response to sensory stimuli after spinal cord injury (SCI)<sup>1</sup>. The fragmented understanding of the mechanisms underlying autonomic dysreflexia hampers the development of therapeutic strategies to manage this condition, leaving people with SCI at daily risk of heart attack and stroke<sup>2–5</sup>. Here we expose the neuronal architecture that develops after SCI and causes autonomic dysreflexia. In parallel, we uncover a competing, yet overlapping neuronal architecture activated by epidural electrical stimulation of the spinal cord that safely regulates blood pressure after SCI. The discovery that these adversarial neuronal architectures converge onto a single neuronal subpopulation provided a blueprint for the design of a mechanism-based intervention that reversed autonomic dysreflexia in mice, rats and humans with SCI. These results establish a path towards essential pivotal device clinical trials that will establish the safety and efficacy of epidural electrical stimulation for the effective treatment of autonomic dysreflexia in people with SCI.

SCI disrupts the communication between the brainstem vasomotor centres and the regions of the spinal cord that regulate haemodynamics<sup>6</sup>. The resulting isolation of neurons in the spinal cord triggers a progressive maladaptive reorganization of neuronal projections throughout the spinal cord below the injury that permits the insidious emergence of uncontrolled hypertensive episodes, known as autonomic dysreflexia<sup>1</sup>. The consequence of these hypertensive episodes is a daily risk of life-threatening cardiovascular events<sup>2–5</sup>.

We reasoned that disentangling the specific neuronal subpopulations involved in the emergence of autonomic dysreflexia, and how these neurons and their projection patterns reorganize after SCI, would uncover key principles to target these neurons therapeutically and thus eliminate autonomic dysreflexia due to SCI.

## Spatial organization of neurons involved in autonomic dysreflexia

In humans with SCI, episodes of autonomic dysreflexia are most commonly triggered by bladder or bowel distension, lower urinary tract infections and pressure sores<sup>7</sup>. We reasoned that identifying the neurons triggering autonomic dysreflexia would require a preclinical model that provokes reliable, repeatable and predictable episodes of autonomic dysreflexia.

To establish this model, we elicited autonomic dysreflexia using colorectal distension in mice<sup>8</sup> with complete upper-thoracic SCI and monitored pressor responses with beat-by-beat blood pressure monitoring (Fig. 1a,b and Extended Data Fig. 1a–d). All mice showed the emergence of autonomic dysreflexia, starting approximately 2 weeks after SCI (Fig. 1c and Extended Data Fig. 1d). The amplitude of these

<sup>1</sup>Department of Clinical Neurosciences, Hotchkiss Brain Institute, Cumming School of Medicine, University of Calgary, Calgary, Alberta, Canada. <sup>2</sup>Department of Cardiac Sciences, Libin Cardiovascular Institute, Cumming School of Medicine, University of Calgary, Calgary, Alberta, Canada. <sup>3</sup>Restore Network, Hotchkiss Brain Institute, Libin Cardiovascular Institute, McCaig Institute for Bone and Joint Health, Cumming School of Medicine, University of Calgary, Calgary, Alberta, Canada. <sup>4</sup>Defitech Center for Interventional Neurotherapies (NeuroRestore), CHUV/UNIL/EPFL, Lausanne, Switzerland. <sup>5</sup>NeuroX Institute, School of Life Sciences, Swiss Federal Institute of Technology (EPFL), Lausanne, Switzerland. <sup>6</sup>Department of Clinical Neuroscience, Lausanne University Hospital (CHUV) and University of Lausanne (UNIL), Lausanne, Switzerland. <sup>7</sup>Lewis-Sigler Institute of Integrative Genomics and Ludwig Institute for Cancer Research, Princeton University, Princeton, NJ, USA. <sup>8</sup>Faculty of Biology and Medicine, University of Lausanne, Lausanne, Switzerland. <sup>9</sup>Wyss Center for Bio and Neuroengineering, Geneva, Switzerland. <sup>10</sup>Department of Physiology and Pharmacology, Cumming School of Medicine, University of Calgary, Calgary, Alberta, Canada. <sup>11</sup>Institute of Science and Technology Brain-inspired Intelligence, Fudan University, Shanghai, China. <sup>12</sup>Laboratory for Soft Bioelectronic Interfaces (LSBI), NeuroX Institute, EPFL, Lausanne, Switzerland. <sup>13</sup>Department of Neurosurgery, Lausanne University Hospital (CHUV) and University of Lausanne (UNIL), Lausanne, Switzerland. <sup>14</sup>These authors contributed equally: Jan Elaine Soriano, Remi Hudelle. <sup>15</sup>These authors jointly supervised this work: Jordan W. Squair, Aaron A. Phillips, Gregoire Courtine. <sup>✉</sup>e-mail: jordan.squair@epfl.ch; aaron.phillips@ucalgary.ca; gregoire.courtine@epfl.ch

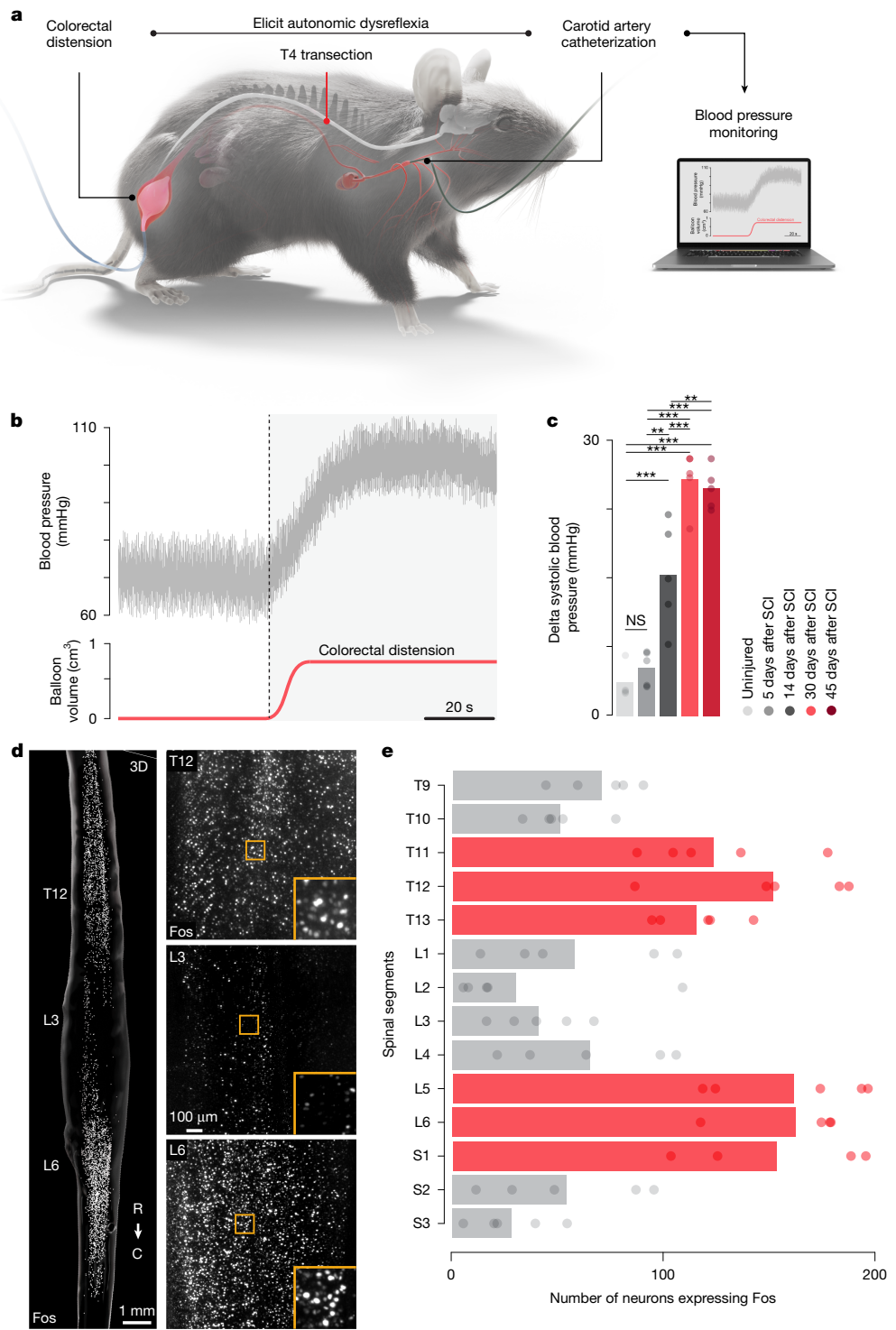


**Fig. 1 | Autonomic dysreflexia triggers transcriptional activity in the lumbosacral and lower thoracic spinal cord.** **a**, Experimental model to quantify the severity of autonomic dysreflexia in mice with complete SCI. **b**, Changes in blood pressure during an episode of autonomic dysreflexia elicited by a controlled colorectal distension (black dashed line). **c**, Severity of autonomic dysreflexia measured by the change in systolic blood pressure elicited by a controlled colorectal distension at different timepoints after SCI (5 days post-injury to uninjured ( $P = 0.95$ ), 14 days post-injury to uninjured ( $P = 0.000048$ ), 30 days post-injury to uninjured ( $P = 0.0000001$ ), 45 days post-injury to uninjured ( $P = 0.0000001$ ), 14 days post-injury to 5 days post-injury ( $P = 0.0013$ ), 30 days post-injury to 5 days post-injury ( $P = 0.0000001$ ), 45 days

post-injury to 5 days post-injury ( $P = 0.0000002$ ), 30 days post-injury to 14 days post-injury ( $P = 0.00086$ ), 45 days post-injury to 14 days post-injury ( $P = 0.0024$ ) and 45 days post-injury to 30 days post-injury ( $P = 0.99$ )). NS, not significant.

**d**, Whole-spinal-cord visualization of immunohistochemical staining for Fos<sup>9,47</sup> in a mouse with SCI that was exposed to repetitive episodes of autonomic dysreflexia. C, caudal; R, rostral. **e**, Barplot reporting the mean number of Fos-labelled neurons for each spinal cord segment quantified in mice with SCI that were exposed to repetitive episodes of autonomic dysreflexia ( $n = 5$ ; mixed-effect linear model;  $P < 0.001$ ), demonstrating a clear enrichment in the lumbosacral and lower thoracic spinal cord. \* $P < 0.05$ , \*\* $P < 0.01$ , \*\*\* $P < 0.001$ .

pressor responses increased gradually during the following weeks until reaching a plateau by 1 month after SCI, which persisted when tested at 6 weeks after SCI (Fig. 1c and Extended Data Fig. 1d).

To identify the regions of the spinal cord activated during autonomic dysreflexia, we conducted whole-spinal-cord clearing<sup>9</sup>, labelling<sup>10,11</sup>, imaging<sup>12</sup> and automated quantification<sup>13</sup> of Fos, a marker of neuronal activity-induced transcription (Fig. 1d and Extended Data Fig. 1e). We quantified this activity-induced transcription in mice that underwent repetitive autonomic dysreflexia over 90 min (ref. 14) (Fig. 1e and Extended Data Fig. 1f).

We found that autonomic dysreflexia triggered massive transcriptional activation throughout the spinal cord (Extended Data Fig. 1f). However, we detected disproportionate enrichments of neuronal activity in two well-defined regions. The first enrichment occurred in the lower lumbosacral segments that receive the sensory afferents conveying information from the colorectal stimulus (Fig. 1d). The second enrichment emerged within the lower thoracic spinal cord, which is referred to as the haemodynamic hotspot<sup>6</sup>. This region hosts a dense concentration of sympathetic preganglionic neurons that access the splanchnic vasculature through ganglionic neurons to elicit powerful pressor responses<sup>6</sup>. We confirmed these segment-specific enrichments of neuronal activity with classical immunofluorescence of Fos on sectioned tissue (Extended Data Fig. 1g). This pattern of neuronal activation was preserved following complete dorsal rhizotomy of lower thoracic segments, excluding the possibility that the robust activation of neurons in the thoracic spinal cord was due to inputs from bowel afferents (Supplementary Note 2).

## The neurons activated by autonomic dysreflexia

We anticipated that understanding the emergence of maladaptive communication between the lumbosacral and lower thoracic spinal cord would be contingent on identifying the neuronal subpopulations in each region that are activated during autonomic dysreflexia.

The neuronal subpopulations embedded within the spinal cord are parcellated into a hierarchical organization that arises from their neurotransmitter expression, developmental transcription factors and projection patterns<sup>15–17</sup>. This hierarchical organization dictates that identifying the neurons involved in specific neurological functions must follow the logical progression along the cardinal classes.

To follow this progression, we first asked whether the neurons embedded in the lumbosacral and lower thoracic spinal cords, and activated during autonomic dysreflexia, exhibited an excitatory or inhibitory phenotype. Our experiments revealed that vGLUT2<sup>ON</sup> neurons located in the lumbosacral spinal cord propel axonal projections to the lower thoracic spinal cord where vGLUT2<sup>ON</sup> neurons are activated and necessary to trigger autonomic dysreflexia (Supplementary Note 1).

vGLUT2<sup>ON</sup> neurons comprise diverse neuronal subpopulations that collectively encompass more than 50% of neurons in the spinal cord<sup>15–17</sup>. Consequently, we felt compelled to descend the hierarchical organization of neurons in the spinal cord to identify the precise neuronal subpopulations that govern the emergence of autonomic dysreflexia. However, this descent is contingent on an atlas that catalogues the molecular perturbation elicited by autonomic dysreflexia across the compendium of neuronal subpopulations in the spinal cord.

To establish this comparative atlas, we profiled the lumbosacral and lower thoracic spinal cord of mice exposed to repetitive episodes of autonomic dysreflexia using single-nucleus RNA sequencing (snRNA-seq)<sup>18</sup>. We obtained high-quality transcriptomes from 64,739 nuclei that were evenly represented across experimental conditions and spatial locations (Extended Data Fig. 3a,b). We identified all of the major cell types of the mouse spinal cord (Extended Data Fig. 3c–k). We then integrated this dataset within our previous atlases of the mouse spinal cord<sup>13,16,17,19,20</sup>, which enabled us to annotate highly specific neuronal subpopulations that parcellated into dorsal versus ventral, excitatory

versus inhibitory and local (*Nfib*) versus long-projecting (*Zfhx3*) populations<sup>15</sup> (Fig. 2a and Extended Data Fig. 3l–n).

To identify the neuronal subpopulations perturbed by autonomic dysreflexia, we applied cell-type prioritization<sup>19,21</sup>. We captured the principle of cell-type prioritization in a machine-learning method called Augur, which identifies cell types undergoing transcriptional responses to a perturbation by ranking cell types that are increasingly more separable within the highly multidimensional space of gene expression. This prioritization exposed Vsx2<sup>ON</sup> excitatory neurons as the most transcriptionally responsive neuronal subpopulation during autonomic dysreflexia (Fig. 2a). Although Vsx2<sup>ON</sup> neuronal subpopulations were prioritized in both the lumbosacral (neurons defined by the expression of *Hoxa10*) and the lower thoracic (*Hoxa7*) spinal cords, the prioritized neurons in the lumbosacral region were consistent with long-projecting Vsx2<sup>ON</sup> neurons, as they expressed the marker *Zfhx3* (SC<sup>Hoxa10::Zfhx3::Vsx2</sup>), whereas the most perturbed neuronal subpopulation in the lower thoracic spinal cord instead expressed markers of locally projecting neurons *Nfib* (SC<sup>Hoxa7::Nfib::Vsx2</sup>)<sup>15</sup> (Fig. 2a and Extended Data Fig. 3m,n).

The transcriptional prioritization of SC<sup>Hoxa7::Nfib::Vsx2</sup> and SC<sup>Hoxa10::Zfhx3::Vsx2</sup> neurons coincided with a pronounced upregulation of synaptic plasticity pathways, neuron projection guidance programs and dendritic arborization – an ensemble of gene programs associated with circuit reorganization and increased neuronal excitability (Extended Data Fig. 3o). Visualization of the activity-dependent marker Fos confirmed the activation of SC<sup>Hoxa10::Zfhx3::Vsx2</sup> and SC<sup>Hoxa7::Nfib::Vsx2</sup> neurons in the lumbosacral and lower thoracic spinal cord, respectively, in response to autonomic dysreflexia (Extended Data Fig. 3p).

Although developmentally defined V2a neurons that express Vsx2 (previously known as *Chx10*)<sup>22</sup> have been implicated in the production of reaching<sup>23</sup> and walking<sup>13,16,17,19,24</sup>, the participation of Vsx2<sup>ON</sup> neuronal subpopulations to the regulation of blood pressure has, to our knowledge, never been demonstrated. Nonetheless, the results of our comparative snRNA-seq experiments dictate that the activation of SC<sup>Hoxa7::Nfib::Vsx2</sup> and SC<sup>Hoxa10::Zfhx3::Vsx2</sup> neurons triggers autonomic dysreflexia.

## The neuronal architecture of autonomic dysreflexia

As autonomic dysreflexia only emerges after SCI, we reasoned that the injury must induce the formation of a maladaptive neuronal architecture that incorporates SC<sup>THORACIC::Vsx2</sup> neurons and SC<sup>LUMBAR::Vsx2</sup> neurons, and possesses the anatomical and functional features compatible with the requirements to trigger autonomic dysreflexia. To expose this architecture, we conducted sequential anatomical and functional experiments that aimed to reconstruct the successive nodes composing the blueprint of the neuronal architecture responsible for autonomic dysreflexia (Fig. 2b,c and Extended Data Fig. 4a).

Small diameter nociceptive afferents act as the primary source of sensory input responsible for triggering autonomic dysreflexia<sup>25,26</sup>. Consequently, nociceptive neurons are positioned as the first node within the neuronal architecture of autonomic dysreflexia, implying that SC<sup>LUMBAR::Vsx2</sup> neurons are likely to receive synaptic projections from these afferents. To expose close appositions from these afferents onto SC<sup>LUMBAR::Vsx2</sup> neurons, we labelled synapses from Calca<sup>ON</sup> axonal projections. Although SC<sup>LUMBAR::Vsx2</sup> neurons in the lumbosacral spinal cord did not receive any Calca<sup>ON</sup> axonal projections in uninjured mice, we found that SCI triggered the invasion of Calca<sup>ON</sup> axons into intermediate laminae, where they established synaptic-like appositions onto SC<sup>LUMBAR::Vsx2</sup> neurons (Fig. 2d and Extended Data Fig. 4b–d). This anatomical reorganization suggested that Calca<sup>ON</sup> neurons trigger autonomic dysreflexia through the activation of SC<sup>LUMBAR::Vsx2</sup> neurons. To expose this causality, we ablated Calca<sup>ON</sup> neurons in the dorsal root ganglia with diphtheria toxin in Calca<sup>Cre::Advl<sup>FloP</sup>::iDTR</sup> mice<sup>27</sup>. The ablation of this afferent subpopulation abolished autonomic dysreflexia. By contrast, the ablation of parvalbumin (PV<sup>ON</sup>) neurons in the dorsal root ganglia, which convey proprioceptive information along large

# Article

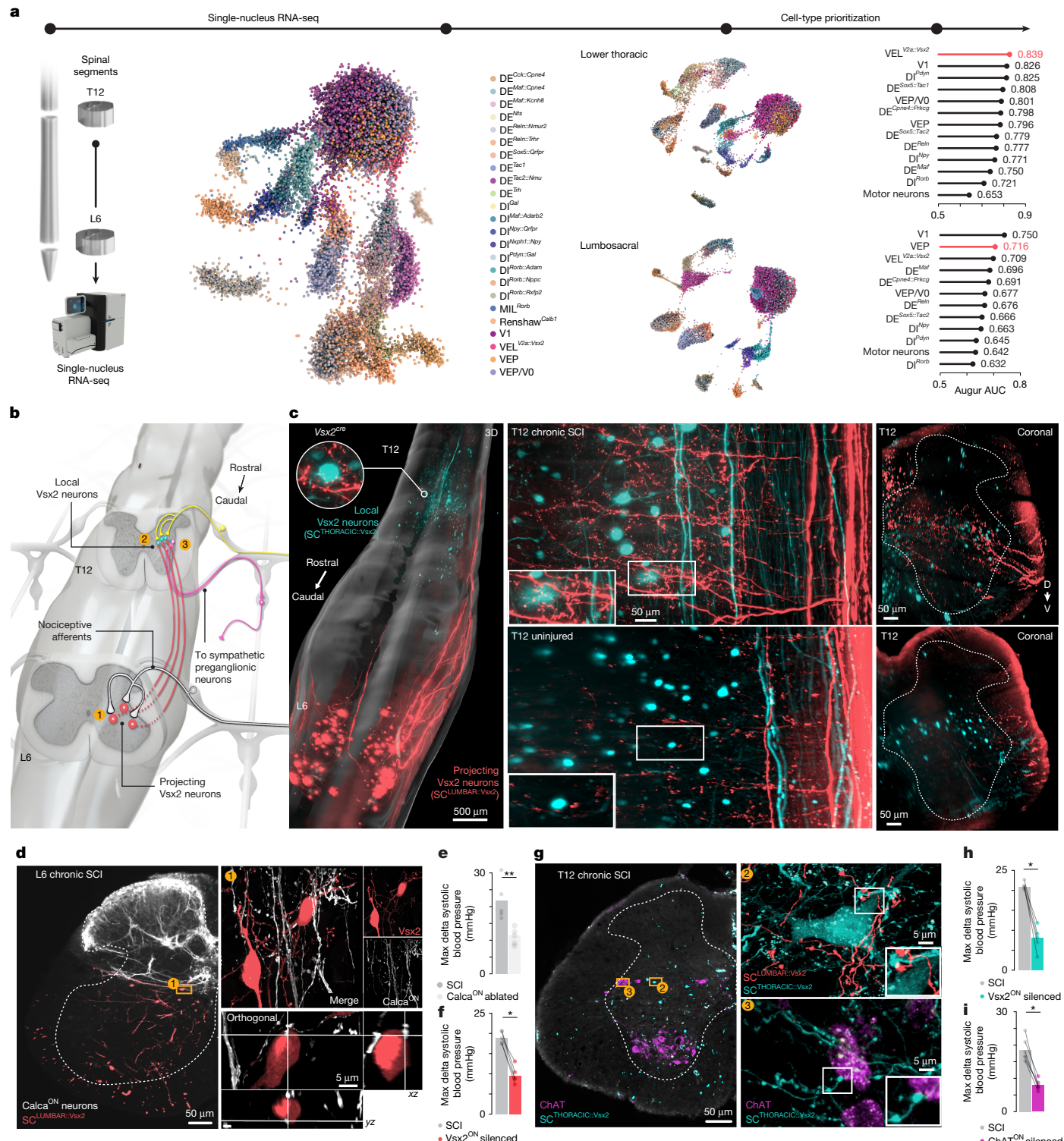


**Fig. 2 |** See next page for caption.

diameter afferents that project into the spinal cord, failed to influence autonomic dysreflexia (Fig. 2e and Extended Data Fig. 4e,f).

We next posited that SC<sup>LUMBAR:Vsx2</sup> act as the second node in the neuronal architecture of autonomic dysreflexia (Fig. 2b,c and Extended Data Fig. 4g,h). To expose the necessity of SC<sup>LUMBAR:Vsx2</sup> neurons in triggering autonomic dysreflexia, we infused AAV5-hSyn-flex-Chrimson-tdTomato<sup>29</sup> into the lumbar spinal cord of Vsx2-Cre mice to express excitatory opsins in SC<sup>LUMBAR:Vsx2</sup> neurons. Optogenetic stimulation of SC<sup>LUMBAR:Vsx2</sup> neurons immediately triggered autonomic dysreflexia. This increase in blood pressure contrasted with the absence of pressor responses when the same optogenetic manipulation of SC<sup>LUMBAR:Vsx2</sup> neurons was performed in uninjured mice (Extended Data Fig. 4l–n).

We then sought to establish the sufficiency of SC<sup>LUMBAR:Vsx2</sup> neurons to trigger autonomic dysreflexia. To expose this sufficiency, we infused AAV5-hSyn-flex-Chrimson-tdTomato<sup>29</sup> into the lumbar spinal cord of Vsx2-Cre mice to express excitatory opsins in SC<sup>LUMBAR:Vsx2</sup> neurons. Optogenetic stimulation of SC<sup>LUMBAR:Vsx2</sup> neurons immediately triggered autonomic dysreflexia. This increase in blood pressure contrasted with the absence of pressor responses when the same optogenetic manipulation of SC<sup>LUMBAR:Vsx2</sup> neurons was performed in uninjured mice (Extended Data Fig. 4l–n).

**Fig. 2 | The neuronal architecture of autonomic dysreflexia.** **a**, Schematic overview of the experiment. Uniform manifold approximation and projection (UMAP) visualization of 64,739 neuronal nuclei, coloured by neuronal subpopulation identity (left). UMAP visualizations of neuronal subpopulations in the lower thoracic (top) and lumbosacral (bottom) spinal cord (middle). Ranking of neuronal subpopulations most responsive to autonomic dysreflexia with Augur (right). AUC, area under the curve; DE, dorsal excitatory; DI, dorsal inhibitory; MIL, middle inhibitory deep laminate; VEL, ventral excitatory local; VEP, ventral excitatory projecting. **b**, Schematic overview of the neuronal architecture of autonomic dysreflexia, including the nodes (numbers) that are dissected anatomically and functionally in the subsequent panels. **c**, Whole-spinal-cord visualization of projections from SC<sup>LUMBAR::Vsx2</sup> neurons located in the lumbosacral spinal cord that project to SC<sup>THORACIC::Vsx2</sup> neurons located in the lower thoracic spinal cord. White dashed lines outline the grey matter. **D**, dorsal; **V**, ventral. **d**, Calca<sup>ON</sup> projections labelled with immunohistochemistry onto SC<sup>LUMBAR::Vsx2</sup> neurons in the lumbosacral spinal cord, including insets showing synaptic-like appositions. **e**, Barplot reporting the severity of autonomic dysreflexia, quantified as the mean change in systolic blood

pressure in response to colorectal distension before and after the ablation of Calca<sup>ON</sup> neurons located in the dorsal root ganglia in Calca<sup>Cre::Avil<sup>Flopo</sup>::iDT</sup> mice ( $n = 5$ ; independent samples  $t$ -test;  $t = -6.0$ ;  $P = 0.0006$ ). **f**, Severity of autonomic dysreflexia before and after chemogenetic silencing of Vsx2<sup>ON</sup> neurons located in the lumbosacral spinal cord in Vsx2-Cre mice ( $n = 5$ ; paired samples  $t$ -test;  $t = -9.47$ ;  $P = 0.00069$ ). **g**, Projections from SC<sup>LUMBAR::Vsx2</sup> in the lower thoracic spinal cord co-labelled with SC<sup>THORACIC::Vsx2</sup> neurons and their local projections as well as immunohistochemical labelling of ChAT<sup>ON</sup> neurons. The insets show synaptic-like appositions from SC<sup>LUMBAR::Vsx2</sup> neurons onto SC<sup>THORACIC::Vsx2</sup> neurons, and synaptic-like appositions of projections from SC<sup>THORACIC::Vsx2</sup> neurons to ChAT<sup>ON</sup> sympathetic preganglionic neurons located in the intermediolateral column. **h**, Severity of autonomic dysreflexia before and after chemogenetic silencing of Vsx2<sup>ON</sup> neurons located in the lower thoracic spinal cord in Vsx2-Cre mice ( $n = 5$ ; paired samples  $t$ -test;  $t = -9.39$ ;  $P = 0.00072$ ). **i**, Severity of autonomic dysreflexia before and after chemogenetic silencing of ChAT<sup>ON</sup> neurons located in the lower thoracic spinal cord in ChAT-Cre mice ( $n = 5$ ; paired samples  $t$ -test;  $t = -8.03$ ;  $P = 0.00048$ ).

The necessity and sufficiency of SC<sup>LUMBAR::Vsx2</sup> neurons to trigger autonomic dysreflexia implied that SCI must also provoke SC<sup>LUMBAR::Vsx2</sup> neurons to propel axonal projections to the lower thoracic spinal cord. To uncover these putative projections, we infused rAAV2-EF1a-DIO-Flopo into the lower thoracic spinal cord followed by infusions of AAV5-hSyn-Con/Fon-eYFP (enhanced yellow fluorescent protein)<sup>30</sup> into the lumbosacral spinal cord of Vsx2-Cre mice. This neuroanatomical tracing strategy exposed long-distance projections from SC<sup>LUMBAR::Vsx2</sup> neurons that established synaptic-like appositions onto SC<sup>THORACIC::Vsx2</sup> neurons in the lower thoracic spinal cord (Fig. 2c and Extended Data Fig. 5a–e). Monosynaptically restricted transsynaptic tracing with avian enveloped G-deleted Rabies confirmed that SC<sup>LUMBAR::Vsx2</sup> neurons established direct synaptic projections onto SC<sup>THORACIC::Vsx2</sup> neurons (Extended Data Fig. 5f).

As SC<sup>THORACIC::Vsx2</sup> neurons in the lower thoracic spinal cord were transcriptionally perturbed by autonomic dysreflexia and received direct synaptic projections from SC<sup>LUMBAR::Vsx2</sup> neurons, we hypothesized that SC<sup>THORACIC::Vsx2</sup> neurons must act as the third node in the neuronal architecture of autonomic dysreflexia (Fig. 2c and Extended Data Fig. 5a–e). To establish the necessity and sufficiency of this node, we manipulated the activity of SC<sup>THORACIC::Vsx2</sup> neurons. Chemogenetic inactivation of these neurons blunted autonomic dysreflexia (Fig. 2g,h and Extended Data Fig. 5g–i). In turn, optogenetic activation of SC<sup>THORACIC::Vsx2</sup> neurons immediately triggered pressor responses (Extended Data Fig. 5j–l).

We next asked whether the projection pattern of SC<sup>THORACIC::Vsx2</sup> neurons in the lower thoracic spinal cord would be compatible with an involvement in autonomic dysreflexia. To answer this question, we infused AAV5-hSyn-flex-tdTomato into Vsx2-Cre mice and quantified the density of projections that formed synaptic-like appositions with ChAT<sup>ON</sup> neurons in the intermediolateral column of lower thoracic spinal segments, where ChAT<sup>ON</sup> sympathetic preganglionic neurons reside (Extended Data Fig. 5m–o). Although SC<sup>THORACIC::Vsx2</sup> neurons primarily projected ventrally, we also detected projections that expanded laterally where they established synaptic-like appositions with the majority of ChAT<sup>ON</sup> neurons located in the intermediolateral column of the lower thoracic spinal cord.

ChAT<sup>ON</sup> sympathetic preganglionic neurons are embedded in the intermediolateral column, and we found that they receive projections from SC<sup>THORACIC::Vsx2</sup> neurons. Consequently, we surmized that ChAT<sup>ON</sup> neurons act as the fourth and final node in the neuronal architecture of autonomic dysreflexia. Indeed, chemogenetic inactivation of ChAT<sup>ON</sup> neurons located in the lower thoracic spinal cord abolished autonomic dysreflexia elicited by bowel distension (Fig. 2h and Extended Data Fig. 5p–r).

These sequential anatomical and functional experiments exposed the neuronal architecture that causes autonomic dysreflexia.

The building blocks of this architecture are precipitated by SCI, in which specific neuronal nodes form maladaptive connections that permit and exacerbate the emergence of autonomic dysreflexia. This architecture has its foundation in Calca<sup>ON</sup> neurons located in the dorsal root ganglia, which establish maladaptive projections to SC<sup>LUMBAR::Vsx2</sup> neurons in the lumbosacral spinal cord. In turn, a SCI provokes these neurons to propel axons to the haemodynamic hotspot located within the lower thoracic spinal cord, where they form synaptic connections with SC<sup>THORACIC::Vsx2</sup> neurons. These locally projecting neurons naturally establish connections onto ChAT<sup>ON</sup> sympathetic preganglionic neurons, which therefore permit massive blood pressure elevations through the recruitment of neurons in splanchnic ganglia and subsequent  $\alpha_1$  receptor activation throughout the dense splanchnic vasculature. The consequence of this aberrant neuronal architecture is the emergence of life-threatening autonomic dysreflexia.

## Competitive neuronal architectures converge on SC<sup>THORACIC::Vsx2</sup> neurons

Our results demonstrate that SCI precipitates the formation of an aberrant neuronal architecture that exploits the natural connections from SC<sup>THORACIC::Vsx2</sup> neurons onto sympathetic preganglionic neurons located in the haemodynamic hotspot to trigger autonomic dysreflexia. We reasoned that competitive engagement of the same neuronal subpopulations with an intervention that mediates beneficial, as opposed to maladaptive reorganization of synaptic projections onto SC<sup>THORACIC::Vsx2</sup> neurons, could prevent the emergence of autonomic dysreflexia. Using molecular cartography, we recently demonstrated that epidural electrical stimulation (EES) of the lumbar spinal cord restores walking through the activation of locally projecting Vsx2<sup>ON</sup> neurons in the lumbar spinal cord<sup>13,19</sup>. We surmized that the same principle must exist in the lower thoracic spinal cord, as we have previously shown that EES applied over this haemodynamic hotspot triggers robust pressor responses after SCI<sup>6</sup>. We thus hypothesized that EES applied over the lower thoracic spinal cord activates SC<sup>THORACIC::Vsx2</sup> neurons, and that EES could thus compete with SC<sup>LUMBAR::Vsx2</sup> neurons to modulate SC<sup>THORACIC::Vsx2</sup> neurons.

To identify the neuronal subpopulations engaged by EES applied to the lower thoracic spinal cord, we performed an additional comparative snRNA-seq experiment (Extended Data Fig. 6a–c). Concretely, we profiled neuronal nuclei from mice with SCI that had received EES over the lower thoracic spinal cord for 30 min. As we have previously described in rats, non-human primates and humans with SCI<sup>6</sup>, all the mice exhibited robust pressor responses when delivering EES over the lower thoracic spinal cord, referred to as the haemodynamic hotspot (Fig. 3a,b). High-quality transcriptional profiles were obtained from

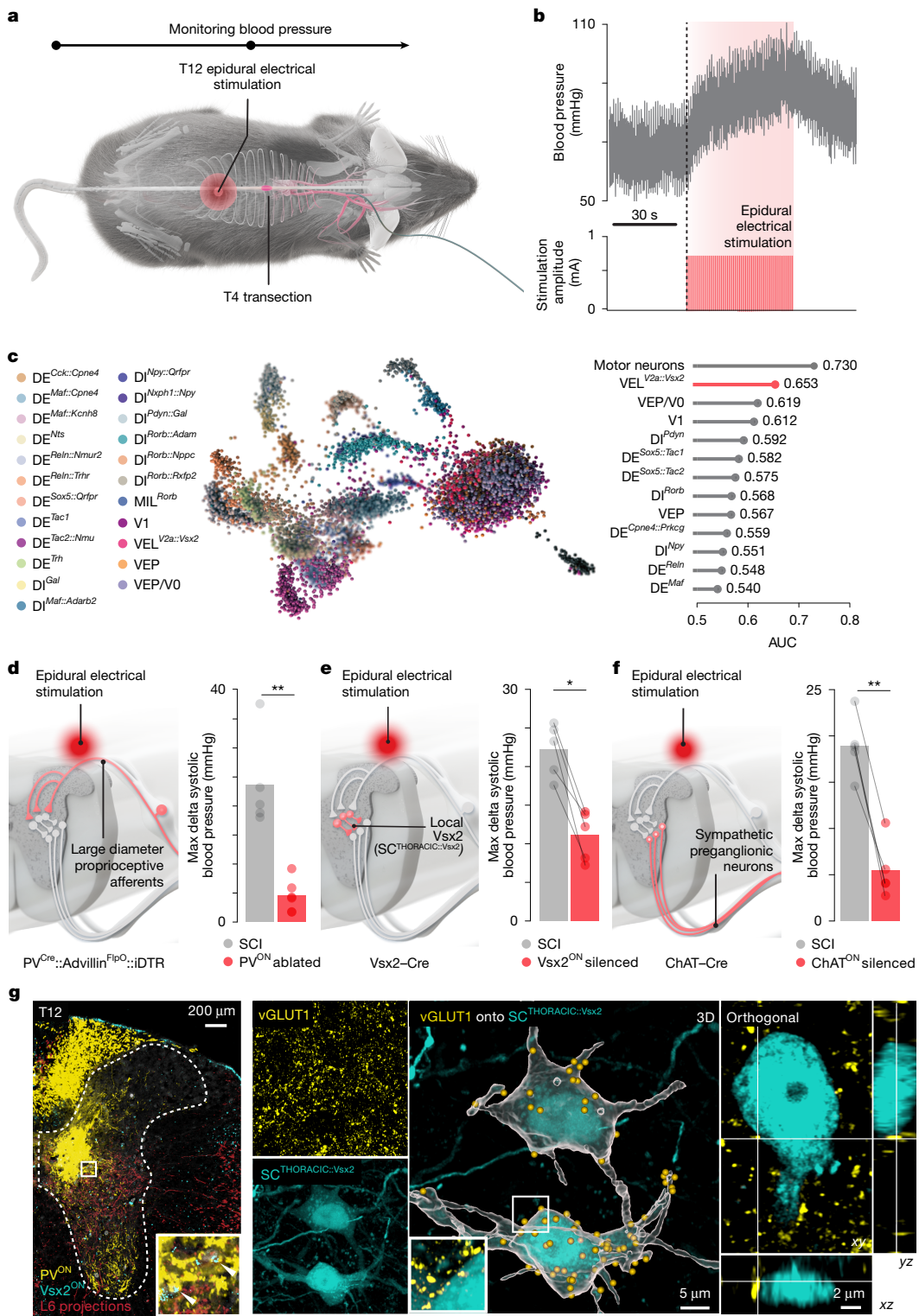


**Fig. 3 | The neuronal architecture of EES-induced pressor responses.**

**a**, Schematic overview of experiments to trigger pressor responses with EES in mice with SCI. **b**, Pressor response induced by continuous (40 Hz) EES (black dashed line) in a mouse with SCI. **c**, UMAP visualization of 21,098 neuronal nuclei, coloured by neuronal subpopulation identity (left). Ranking of neuronal subpopulations most responsive to EES with Augur (right). **d–f**, Schematic overview of the successive nodes constituting the neuronal architecture through which EES applied over the lower thoracic spinal cord induces pressor responses. EES-induced pressor responses before and after the ablation of PV<sup>ON</sup> neurons located in the dorsal root ganglia in PV<sup>Cre::AdvilFlpO::iDTR</sup> mice ( $n = 5$ ; independent samples  $t$ -test;  $t = -5.41$ ;  $P = 0.0043$ ; **d**). EES-induced pressor responses before

and after chemogenetic silencing of Vsx2<sup>ON</sup> neurons located in the lower thoracic spinal cord in Vsx2-Cre mice ( $n = 5$ ; paired samples  $t$ -test;  $t = -4.21$ ;  $P = 0.014$ ; **e**). EES-induced pressor responses before and after chemogenetic silencing of ChAT<sup>ON</sup> neurons located in the lower thoracic spinal cord in ChAT-Cre mice ( $n = 5$ ; paired samples  $t$ -test;  $t = -7.07$ ;  $P = 0.0021$ ; **f**). **g**, Photomicrograph of the lower thoracic spinal cord demonstrating vGLUT1 synaptic puncta and synaptic-like appositions from large-diameter afferent neurons onto SC<sup>THORACIC::Vsx2</sup> neurons labelled with *in situ* hybridization (left) or viral tract tracing (right) in the lower thoracic spinal cord of PV<sup>Cre::AdvilFlpO::tdTomato</sup> mice. Arrowheads mark PV<sup>ON</sup> synaptic-like appositions and L6 projections onto Vsx2<sup>ON</sup> neurons. White dashed lines outline the grey matter.

21,098 nuclei (Fig. 3c). Integration of this dataset<sup>31</sup> with our previous atlases<sup>13,16,17,19,20</sup> and data from the experiments conducted on mice that were exposed to repetitive autonomic dysreflexia enabled us to identify and evaluate the same neuronal subpopulations. Cell-type prioritization<sup>19,21</sup> revealed that locally projecting SC<sup>Hoxa7::Nfib::Vsx2</sup> neurons exhibited the most pronounced transcriptional response across the compendium of neuronal subpopulations embedded in the lower thoracic spinal cord of mice that had received EES targeting the haemodynamic hotspot (Fig. 3c and Extended Data Fig. 6d,e).

As we have previously found that Vsx2<sup>ON</sup> neurons were recruited in response to EES in the lumbar spinal cord<sup>13,19</sup>, these comparative snRNA-seq experiments indicate that the principle through which EES recruits specific neuronal subpopulations is conserved across the thoracolumbar spinal cord. Moreover, this observation nominates SC<sup>Hoxa7::Nfib::Vsx2</sup> neurons as a convergence node that is not only recruited during autonomic dysreflexia but can also be engaged by the neuronal architecture that prevents orthostatic hypotension when the delivery of EES targets the haemodynamic hotspot.

The discovery of this intersection compelled us to expose the entire neuronal architecture activated by EES. Therefore, we conducted sequential anatomical and functional experiments that aimed to reconstruct the successive nodes involved in the pressor responses during the delivery of EES targeting the haemodynamic hotspot.

We have previously shown that EES applied over the lower thoracic spinal cord activates afferent fibres in the posterior roots to trigger pressor responses<sup>6</sup>, and mounting evidence suggests that EES restores walking through the recruitment of large-diameter afferent fibres where they bend to enter the lumbosacral spinal cord through the dorsal root entry zones<sup>32,33</sup>. We thus asked whether large-diameter afferent neurons act as the first node of the neuronal architecture that enables EES targeting the haemodynamic hotspot to trigger pressor responses (Extended Data Fig. 7a,b).

To answer this question, we ablated proprioceptive or nociceptive neurons with the administration of diphtheria toxin to PV<sup>Cre::Advl</sup><sup>FloP::iDTR</sup> mice and Calca<sup>Cre::Advl</sup><sup>FloP::iDTR</sup> mice, and applied EES targeting the haemodynamic hotspot. The ablation of PV<sup>ON</sup> neurons in the dorsal root ganglia abolished pressor responses to EES, whereas the ablation of Calca<sup>ON</sup> neurons had no effect (Fig. 3d and Extended Data Fig. 7b–d). We then verified that large-diameter afferents establish synaptic projections onto SC<sup>THORACIC::Vsx2</sup> neurons in the lower thoracic spinal cord. To expose this connectome, we visualized large-diameter afferent fibres in PV<sup>Cre::Advl</sup><sup>FloP::Ai9(RCL-tdT)</sup> mice and confirmed that these fibres established vGLUT1<sup>ON</sup> synaptic appositions onto SC<sup>THORACIC::Vsx2</sup> neurons (Extended Data Fig. 7e–g). The dense projections from PV<sup>ON</sup> neurons onto SC<sup>THORACIC::Vsx2</sup> neurons contrasted with the absence of projections from PV<sup>ON</sup> neurons onto ChAT<sup>ON</sup> neurons in the intermediolateral column of the lower thoracic spinal cord, both before and after SCI (Extended Data Fig. 7e–g). Monosynaptically restricted trans-synaptic tracing with avian enveloped G-deleted Rabies confirmed that PV<sup>ON</sup> neurons in the dorsal root ganglia established direct synaptic projections onto SC<sup>THORACIC::Vsx2</sup> neurons (Extended Data Fig. 7h).

As SC<sup>Hoxa7::Nfib::Vsx2</sup> neurons underwent the greatest transcriptional perturbation following EES targeting the haemodynamic hotspot and receive direct projections from large-diameter afferent fibres that are recruited by EES, we anticipated that SC<sup>THORACIC::Vsx2</sup> neurons act as the second node in the neuronal architecture that enables EES to trigger pressor responses. To expose the necessary role of SC<sup>THORACIC::Vsx2</sup> neurons, we infused AAV5-hSyn-DIO-hM4Di-mCherry into the lower thoracic spinal cords of Vsx2-Cre mice. Inactivation of SC<sup>THORACIC::Vsx2</sup> neurons blunted the pressor responses triggered by EES (Fig. 3e and Extended Data Fig. 7i,j).

We surmised that ChAT<sup>ON</sup> sympathetic preganglionic neurons would logically act as the third and final node in the neuronal architecture that enables EES targeting the haemodynamic hotspot to trigger pressor responses. Indeed, chemogenetic inactivation of ChAT<sup>ON</sup> neurons

located in the lower thoracic spinal cord abolished pressor responses triggered by EES (Fig. 3f and Extended Data Fig. 7k,l).

Together, these results uncovered the neuronal architecture that enables EES targeting the haemodynamic hotspot of the lower thoracic spinal cord to trigger pressor responses. EES directly recruits large diameter afferents to activate SC<sup>THORACIC::Vsx2</sup> neurons, which project to ChAT<sup>ON</sup> sympathetic preganglionic neurons to elicit pressor responses through the activation of ganglionic neurons, and subsequent α<sub>1</sub> receptor activation to induce vasoconstriction.

Finally, we surmized that for the neuronal architecture enabling EES to elicit pressor responses to compete with the neuronal architecture that triggers autonomic dysreflexia, these two architectures must intersect on the same SC<sup>THORACIC::Vsx2</sup> neurons in the lower thoracic spinal cord.

To expose this anatomical and functional intersection, we first infused AAV5-hSyn-GFP into the lumbosacral spinal cord of PV<sup>Cre::Advl</sup><sup>FloP::Ai9(RCL-tdT)</sup> mice with SCI coupled to labelling of SC<sup>THORACIC::Vsx2</sup> neurons. We found that the same SC<sup>THORACIC::Vsx2</sup> neurons received direct projections from large-diameter afferents emanating from PV<sup>ON</sup> neurons located in dorsal root ganglia and from axons projecting from the lumbosacral spinal cord after SCI (Fig. 3g). Second, we aimed to confirm that these two distinct axonal projections were able to regulate the activity of the same SC<sup>THORACIC::Vsx2</sup> neurons. We conducted single-unit recordings of optogenetically identified SC<sup>THORACIC::Vsx2</sup> neurons in the lower thoracic spinal cord in response to autonomic dysreflexia and EES (Extended Data Fig. 7m). We found that both paradigms elicited short-latency responses in the recorded SC<sup>THORACIC::Vsx2</sup> neurons that were compatible with a direct activation of the same SC<sup>THORACIC::Vsx2</sup> neurons (Extended Data Fig. 7n,o).

## Neuronal architecture competition to reverse autonomic dysreflexia

The intersection between the neuronal architecture that enables EES targeting the haemodynamic hotspot to mediate beneficial elevation of blood pressure and the neuronal architecture that triggers autonomic dysreflexia opened the intriguing possibility that the sustained modulation of SC<sup>THORACIC::Vsx2</sup> neurons with EES could compete with the detrimental activity emanating from aberrant axonal projections of SC<sup>LUMBAR::Vsx2</sup> neurons, ultimately reversing autonomic dysreflexia.

To test this possibility, we subjected mice to autonomic neurorehabilitation, which consisted of daily sessions during which EES targeting the haemodynamic hotspot was delivered over the lower thoracic spinal cord during the course of 1 month (Fig. 4a and Extended Data Fig. 8a). Autonomic neurorehabilitation abolished autonomic dysreflexia in all tested mice (Fig. 4b and Extended Data Fig. 8b).

We suspected that the suppression of autonomic dysreflexia would emerge from the competitive advantage of large-diameter fibre projections over aberrant axonal projections from SC<sup>LUMBAR::Vsx2</sup> neurons to form synaptic connections with SC<sup>THORACIC::Vsx2</sup> neurons (Fig. 4c). To expose this adversarial anatomy, we labelled SC<sup>THORACIC::Vsx2</sup> and SC<sup>LUMBAR::Vsx2</sup> neurons with intersectional viral tracing strategies. We then quantified the relative density of synaptic appositions onto SC<sup>THORACIC::Vsx2</sup> neurons, both vGLUT1 synapses emanating from PV<sup>ON</sup> large-diameter afferent fibres and axonal projections from SC<sup>LUMBAR::Vsx2</sup> neurons. Autonomic neurorehabilitation reduced the number of aberrant projections from SC<sup>LUMBAR::Vsx2</sup> neurons onto SC<sup>THORACIC::Vsx2</sup> neurons, while concomitantly augmenting the density of vGLUT1<sup>ON</sup> synaptic appositions onto SC<sup>THORACIC::Vsx2</sup> neurons embedded in the haemodynamic hotspot (Fig. 4d and Extended Data Fig. 8c,d).

## Mistargeted stimulation exacerbates autonomic dysreflexia

Recent case studies have reported transient increases in blood pressure in response to EES applied over the lumbosacral spinal cord of

# Article

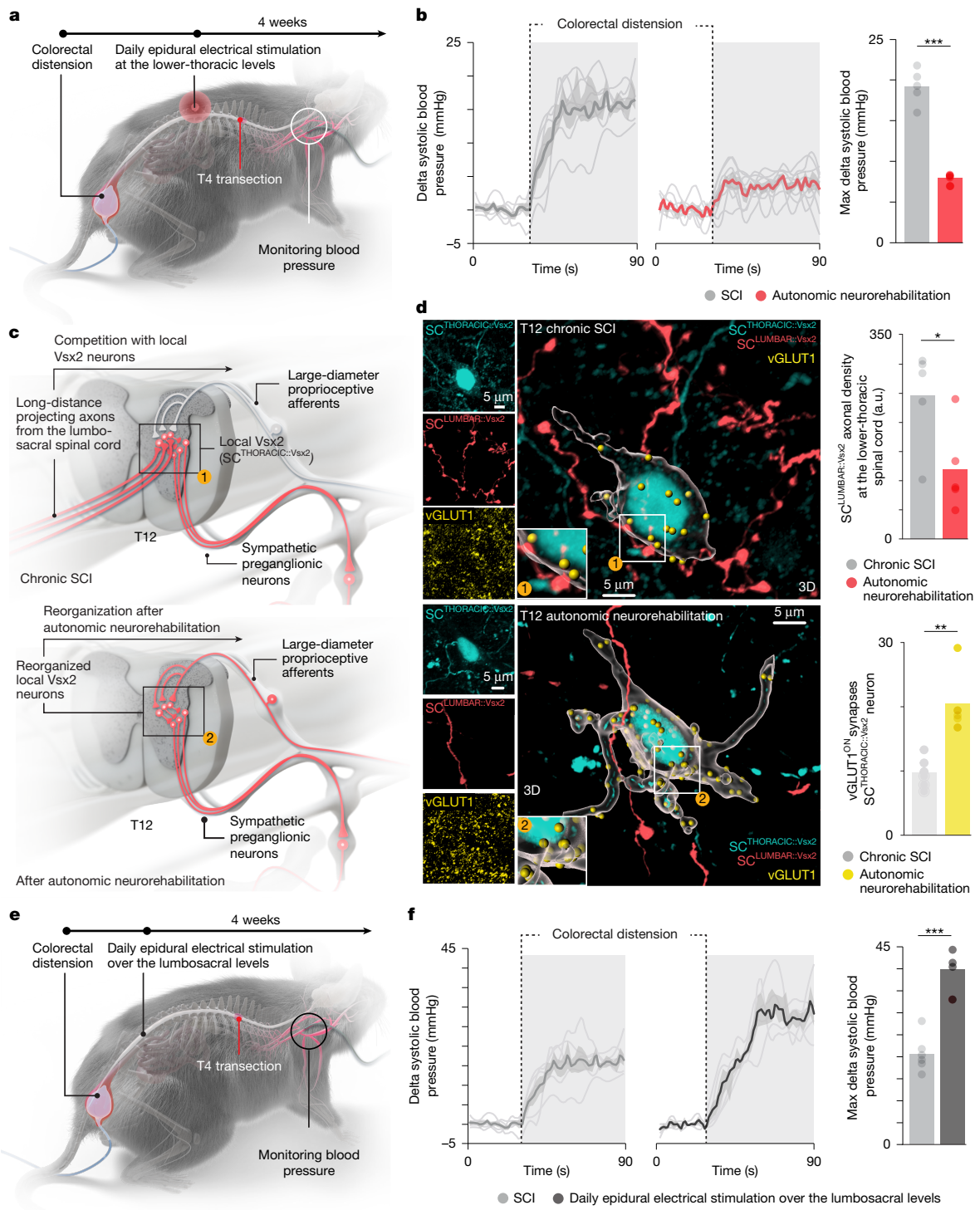


**Fig. 4 | Competitive neuronal architectures converge on SC<sup>THORACIC::Vsx2</sup> neurons.** **a**, Schematic overview of autonomic neurorehabilitation and the paradigm to quantify the severity of autonomic dysreflexia. **b**, Pressor responses (left; individual mice and mean trace) and severity of autonomic dysreflexia (right) in five mice with chronic SCI and five mice that underwent autonomic neurorehabilitation for 4 weeks, starting 1 week after SCI (independent samples *t*-test;  $t = -7.45$ ;  $P = 0.000056$ ). **c**, Schematic overview illustrating the competitive (overlapping) neuronal architectures of autonomic dysreflexia and EES-induced pressor responses, and their rearrangement after autonomic neurorehabilitation. **d**, vGLUT1<sup>ON</sup> synaptic puncta and synaptic-like appositions from SC<sup>LUMBAR::Vsx2</sup> neurons onto SC<sup>THORACIC::Vsx2</sup> neurons in mice with SCI and mice with SCI that underwent autonomic neurorehabilitation.

The barplots report the mean density of axonal projections from SC<sup>LUMBAR::Vsx2</sup> neurons in the thoracic spinal cord in mice with SCI and mice with SCI that underwent autonomic neurorehabilitation ( $n = 5$ ; independent samples *t*-test;  $t = 2.51$ ;  $P = 0.0369$ ; top). The barplots also report the mean number of vGLUT1<sup>ON</sup> synaptic puncta apposing SC<sup>THORACIC::Vsx2</sup> neurons ( $n = 5$ ; independent samples *t*-test;  $t = 4.44$ ;  $P = 0.0055$ ; bottom). **e**, Schematic overview of experiments in which EES was applied daily over the lumbosacral spinal cord of mice with SCI, and the paradigm to quantify the severity of autonomic dysreflexia. **f**, As in panel **b**, but for mice with SCI that were subjected to the daily application of EES over the lumbosacral spinal cord ( $n = 5$ ; independent samples *t*-test;  $t = 5.82$ ;  $P = 0.000070$ ). Grey shaded region indicates the colorectal distension period.

people with SCI<sup>34–39</sup>, and that the long-term delivery of EES over this location led to improvements in resting hypotension and orthostatic hypotension in these individuals. As a paucity of neurons involved in the control of blood pressure reside in the lumbosacral spinal cord, the activation and reinforcement of the neuronal architecture that causes autonomic dysreflexia is the most likely mechanism to account for these observations. Therefore, we hypothesized that the daily activation of SC<sup>LUMBAR::Vsx2</sup> neurons in response to EES applied over the lower lumbosacral spinal cord would provide a competitive advantage to vGLUT2<sup>ON</sup> synapses emanating from these neurons and projecting onto SC<sup>LUMBAR::Vsx2</sup> neurons compared with vGLUT1<sup>ON</sup> synapses received from local PV<sup>ON</sup> large-diameter afferent fibres, and that, ultimately, this shift in the synaptic innervations of SC<sup>LUMBAR::Vsx2</sup> neurons would exacerbate autonomic dysreflexia.

To test this hypothesis, we subjected a new cohort of mice to daily exposure to EES, but instead of delivering EES over the lower thoracic spinal cord to target the haemodynamic hotspot, we applied EES over the lower lumbosacral spinal cord for 30 min during the course of 1 month (Fig. 4e and Extended Data Fig. 8e). This mistargeted stimulation doubled the severity of autonomic dysreflexia in all tested mice (Fig. 4f and Extended Data Fig. 8f). As anticipated, we observed a concomitant increase in the density of axonal projections from SC<sup>LUMBAR::Vsx2</sup> neurons onto SC<sup>THORACIC::Vsx2</sup> neurons, combined with a decrease in the density of vGLUT1 synapses from PV<sup>ON</sup> large-diameter afferent fibres (Extended Data Fig. 8g,h).

The dramatic exacerbation of autonomic dysreflexia triggered by the mistargeted delivery of EES demonstrates that attempts to restore haemodynamic stability with EES applied over the lumbosacral spinal cord are not only less efficacious than EES targeting the haemodynamic hotspot located in the lower thoracic spinal cord<sup>40</sup> but also proved unsafe, as the mechanism by which haemodynamics can be modulated when stimulating this region is by triggering and reinforcing the severity of life-threatening autonomic dysreflexia.

## Longitudinal monitoring of autonomic neurorehabilitation

Although autonomic neurorehabilitation suppressed autonomic dysreflexia in mice, we recognized that the longitudinal monitoring of the safety and efficacy of this treatment over a long period of time would be important to inform the design of a therapy for people living with SCI.

We therefore leveraged our chronic rat model of high-thoracic contusion SCI that enables 24/7 monitoring of haemodynamic parameters without the constraints of tethered electronics<sup>6–41</sup>, which we combined with our electronic dura mater (e-dura<sup>42</sup>) implant optimized to target the haemodynamic hotspot (Extended Data Fig. 9a and Supplementary Note 3).

Rats with SCI were exposed to daily sessions of autonomic neurorehabilitation. Although all tested rats developed autonomic dysreflexia during the first few weeks after SCI, autonomic neurorehabilitation led to the gradual elimination of this symptom (Extended Data Fig. 9b,c). Anatomical examinations confirmed that autonomic neurorehabilitation enabled large-diameter afferents to compete for the innervation of Vsx2<sup>ON</sup> neurons located in the haemodynamic hotspot and, ultimately, to overcome the aberrant neuronal architecture responsible for autonomic dysreflexia (Extended Data Fig. 9d–h). We concluded that autonomic neurorehabilitation is a safe and efficacious treatment to reduce the severity of autonomic dysreflexia in rodents.

## Clinical necessity of therapies for autonomic neurorehabilitation

The neurosurgical intervention necessary to treat autonomic dysreflexia with EES must be weighed against the risks and benefits of the procedure. Establishing this balance requires an understanding of the

prevalence, symptomatology and effectiveness of current management strategies.

Consequently, we leveraged two large-scale surveys on self-reported information on the presence of symptoms of autonomic dysreflexia and demographic information about the level of SCI ( $n = 1,733$  total)<sup>43,44</sup>. These data revealed that 82% of individuals with tetraplegia had been told by a medical practitioner that they present with autonomic dysreflexia. We found that only 30% of the individuals were being treated for autonomic dysreflexia, yet 98% of these treated individuals still experienced symptoms (Fig. 5a and Extended Data Fig. 10a). These symptoms were primarily characterized by vasogenic manifestations including headaches and heart palpitations, sudomotor manifestations including goosebumps and sweating, as well as anxiety (Fig. 5b and Extended Data Fig. 10b–d).

This symptomatology combined with the risk of life-threatening episodes of autonomic dysreflexia and the absence of adequate therapeutic management justified evaluating the effect of autonomic neurorehabilitation on the severity of autonomic dysreflexia in humans living with chronic SCI.

## Preliminary clinical validation of autonomic neurorehabilitation

We next conducted a preliminary clinical evaluation to assess whether the long-term application of EES targeting the haemodynamic hotspot to reduce hypotensive symptomatology also reduces the severity of autonomic dysreflexia in humans with chronic SCI. To carry out this assessment, we leveraged three ongoing observational clinical studies (STIMO-HEMO (NCT04994886, CHUV, Lausanne, Switzerland), HEMO (NCT05044923, University of Calgary, Calgary, Canada) and HemON (NCT05111093, CHUV, Lausanne, Switzerland)) focused on the development of a purpose-built implantable neurostimulation platform to restore haemodynamic stability based on EES targeting the haemodynamic hotspot<sup>40</sup> (Extended Data Fig. 10f).

These studies enrolled patients with cervical SCI who presented with medically refractory orthostatic hypotension. When exposed to orthostatic challenges during a tilt-table test, all the participants exhibited a rapid decline in blood pressure that required the early termination of the tilt test. Following this verification of their eligibility, the participants underwent a neurosurgical intervention to implant an electrode array targeting the dorsal root entry zones innervating the last three thoracic segments and a neurostimulator to deliver EES (Fig. 5c). Post-operative evaluations confirmed that EES targeting the haemodynamic hotspot elicited robust pressor responses that reduced the severity of orthostatic hypotension (Fig. 5d,e). The participants then learned how to operate the therapy to regulate their blood pressure throughout the day for up to 2 years (Extended Data Fig. 10f). During this time, no serious device-related adverse events occurred<sup>40</sup>.

Although these studies focused on the long-term reduction of hypotensive symptomatology, the severity of autonomic symptoms was assessed concurrently with the autonomic dysfunction following SCI (ADFSI) rating scale<sup>45</sup>. Consequently, the context of these studies allowed us to assess how the symptomatology related to autonomic dysreflexia evolved in nine participants.

Quantification of the autonomic dysreflexia subscore within the ADFSI revealed a decrease in symptomatology related to autonomic dysreflexia after long-term use of EES targeting the haemodynamic hotspot. Secondary analyses of vasogenic and sudomotor manifestations revealed that the long-term use of EES targeting the haemodynamic hotspot led to a reduction in headaches and heart palpitations, which are the main vasogenic symptoms of autonomic dysreflexia (Fig. 5f,g and Extended Data Fig. 10g). By stark contrast, sudomotor manifestations and anxiety remained unchanged from baseline.

These clinical outcomes provide preliminary evidence that the daily application of EES targeting the haemodynamic hotspot reduces the

# Article

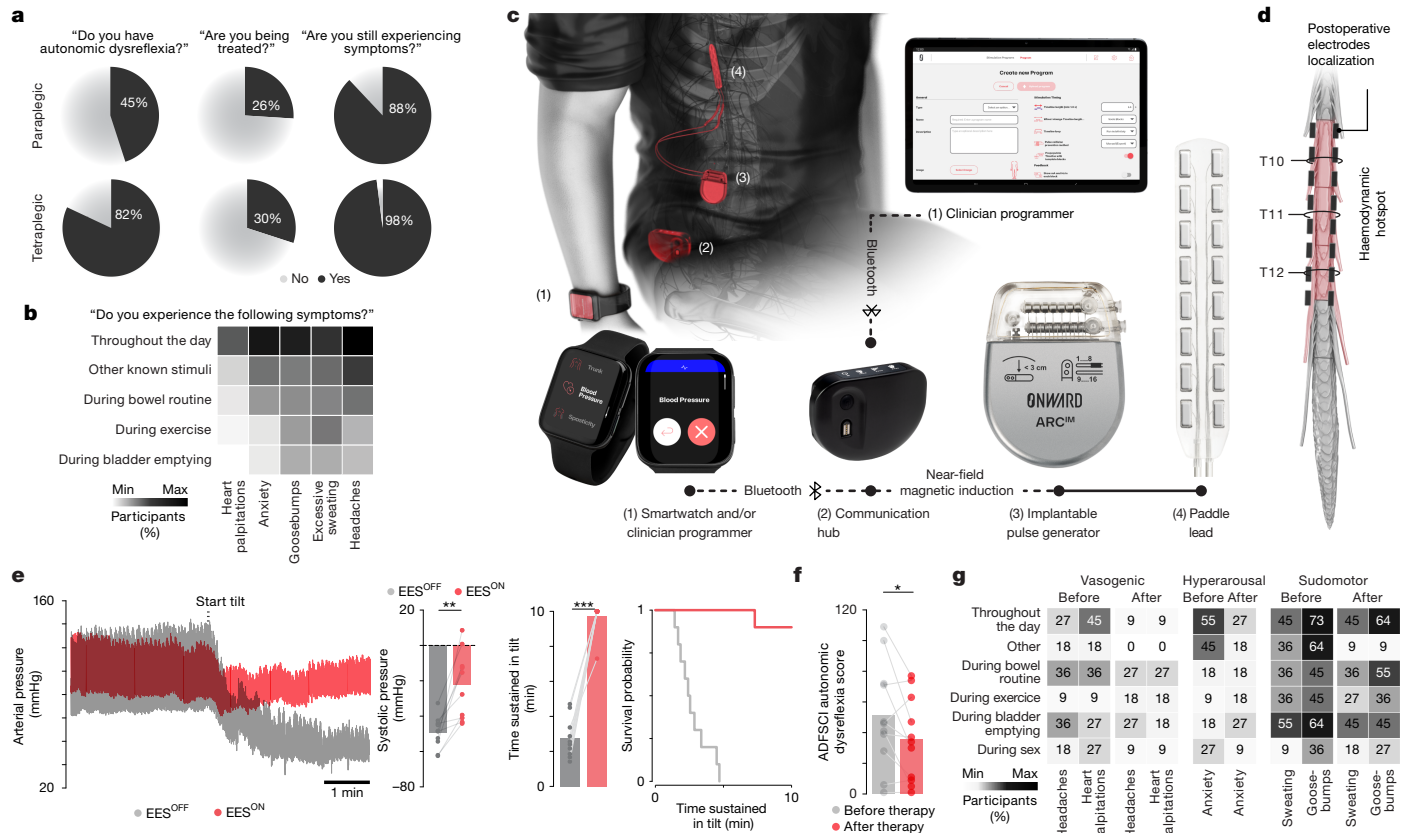


**Fig. 5 | Reduced severity of autonomic dysreflexia in people with chronic SCI following EES targeting the haemodynamic hotspot.** **a**, Prevalence of autonomic dysreflexia and management efficacy quantified in 1,479 individuals with SCI from the Rick Hansen Spinal Cord Injury Registry<sup>43,44</sup>. **b**, Percentage of individuals with tetraplegia experiencing each symptom of autonomic dysreflexia scored in the ADFSCI across various daily activities ( $n = 107$ ). **c**, Implantable system to regulate blood pressure with EES, including a paddle lead with optimized electrode configurations to target the dorsal roots projecting to the haemodynamic hotspot, an implantable pulse generator, communication hub and external smartwatch to operate the various programs of the therapy. **d**, Post-operative reconstruction of the final position of the electrodes following the implantation of the paddle lead. **e**, Changes in blood pressure from a representative participant during an orthostatic challenge

without EES and with continuous EES applied over the haemodynamic hotspot. The barplots report the average drop in systolic blood pressure during orthostatic challenge ( $n = 11$ , paired samples two-tailed  $t$ -test;  $t = 4.7774$ ;  $P = 0.00101$ ) and the average tilt duration without EES and with EES applied over the haemodynamic hotspot ( $n = 11$ , paired samples two-tailed  $t$ -test;  $t = 14.3310$ ;  $P < 0.001$ ). The Kaplan–Meier plot shows exposure status to time, segregated by the presence or absence of EES. Data are derived from a companion article<sup>40</sup>. **f**, ADFSCI autonomic dysreflexia score before implantation and after at least 6 months but up to 2 years after implantation of the system and daily use to regulate blood pressure ( $n = 11$ , paired samples one-tailed  $t$ -test;  $t = 2.3256$ , d.f. = 10,  $P = 0.02118$ ). **g**, Percentage of individuals ( $n = 11$ ) experiencing each symptom described in the ADFSCI autonomic dysreflexia section before implantation (before) and at the latest timepoint of ARC<sup>TM</sup> therapy (after).

severity of autonomic dysreflexia in humans with chronic SCI, as quantified functionally and anatomically in mice and rats.

## Discussion

Here we exposed the complete, aberrant neuronal architecture that develops after SCI and causes autonomic dysreflexia. Although all the neurons constituting this neuronal architecture exists in healthy mice, the SCI precipitates the development of connections between nociceptive neurons and *Vsx2*-expressing neurons, as well as between *Vsx2*-expressing neurons located in the lumbosacral and lower thoracic spinal cord that provoke the emergence of autonomic dysreflexia. This architecture incorporates locally projecting, *Vsx2*-expressing neurons located in the lower thoracic spinal cord that are also embedded in the neuronal architecture that enables EES targeting the haemodynamic hotspot to achieve safe and well-controlled increases of blood pressure. As these adversarial architectures converged onto a single neuronal subpopulation, their relative activation determined the prevailing architecture in this competitive interaction.

Exposing these adversarial architectures allowed us to design a safe intervention that reversed autonomic dysreflexia in mice, rats and

humans with SCI by applying EES targeting the haemodynamic hotspot located in the lower thoracic spinal cord. Conversely, the mistargeted application of EES over the lumbosacral spinal cord reinforced the anatomical and functional connectivity of the neuronal architecture responsible for autonomic dysreflexia, which augmented the severity of these symptoms.

People living with SCI and medical practitioners are taught to identify warning signs such as headaches, sweating and goosebumps, as these signs indicate the presence of a noxious stimulus that is triggering autonomic dysreflexia, which must therefore be localized to resolve the ongoing hypertensive episode as quickly as possible<sup>40</sup>. Analysis of self-reported symptoms in patients from four clinical studies showed that EES targeting the haemodynamic hotspot reduced headaches and heart palpitations, which are both directly related to dangerous increases in blood pressure. Instead, this therapy had no detectable effect on the other warning signs such as goosebumps and sweating that could still inform on the presence of noxious stimulus.

We took advantage of ongoing clinical trials to collect preliminary evidence on the potential for EES targeting the haemodynamic hotspot to reduce autonomic dysreflexia in humans with SCI. However, these trials were not designed to demonstrate the safety and efficacy

of this therapy, and relied only on self-reported symptoms instead of physiological outcomes. Consequently, the next steps must include the assessment of the safety and efficacy of EES targeting the haemodynamic hotspot to reduce autonomic dysreflexia in a pivotal device trial.

## Online content

Any methods, additional references, Nature Portfolio reporting summaries, source data, extended data, supplementary information, acknowledgements, peer review information; details of author contributions and competing interests; and statements of data and code availability are available at <https://doi.org/10.1038/s41586-025-09487-w>.

1. Phillips, A. A. & Krassioukov, A. V. Contemporary cardiovascular concerns after spinal cord injury: mechanisms, maladaptations, and management. *J. Neurotrauma* **32**, 1927–1942 (2015).
2. Squair, J. W., Phillips, A. A., Harmon, M. & Krassioukov, A. V. Emergency management of autonomic dysreflexia with neurologic complications. *Can. Med. Assoc. J.* **188**, 1100–1103 (2016).
3. Wan, D. & Krassioukov, A. V. Life-threatening outcomes associated with autonomic dysreflexia: a clinical review. *J. Spinal Cord Med.* **37**, 2–10 (2014).
4. Cragg, J. J., Noonan, V. K., Krassioukov, A. & Borisoff, J. Cardiovascular disease and spinal cord injury: results from a national population health survey. *Neurology* **81**, 723–728 (2013).
5. Wu, J.-C. et al. Increased risk of stroke after spinal cord injury: a nationwide 4-year follow-up cohort study. *Neurology* **78**, 1051–1057 (2012).
6. Squair, J. W. et al. Neuroprosthetic baroreflex controls haemodynamics after spinal cord injury. *Nature* **590**, 308–314 (2021).
7. Teasell, R. W., Arnold, J. M., Krassioukov, A. & Delaney, G. A. Cardiovascular consequences of loss of supraspinal control of the sympathetic nervous system after spinal cord injury. *Arch. Phys. Med. Rehabil.* **81**, 506–516 (2000).
8. Mayorov, D. N., Adams, M. A. & Krassioukov, A. V. Telemetric blood pressure monitoring in conscious rats before and after compression injury of spinal cord. *J. Neurotrauma* **18**, 727–736 (2001).
9. Renier, N. et al. Mapping of brain activity by automated volume analysis of immediate early genes. *Cell* **165**, 1789–1802 (2016).
10. Bullitt, E. Expression of c-Fos-like protein as a marker for neuronal activity following noxious stimulation in the rat. *J. Comp. Neurol.* **296**, 517–530 (1990).
11. Sheng, M. & Greenberg, M. E. The regulation and function of c-Fos and other immediate early genes in the nervous system. *Neuron* **4**, 477–485 (1990).
12. Tomer, R., Ye, L., Hsueh, B. & Deisseroth, K. Advanced CLARITY for rapid and high-resolution imaging of intact tissues. *Nat. Protoc.* **9**, 1682–1697 (2014).
13. Kathe, C. et al. The neurons that restore walking after paralysis. *Nature* **611**, 540–547 (2022).
14. Ueno, M., Ueno-Nakamura, Y., Niehaus, J., Popovich, P. G. & Yoshida, Y. Silencing spinal interneurons inhibits immune suppressive autonomic reflexes caused by spinal cord injury. *Nat. Neurosci.* **19**, 784–787 (2016).
15. Osseward, P. J. et al. Conserved genetic signatures parcellate cardinal spinal neuron classes into local and projection subsets. *Science* **372**, 385–393 (2021).
16. Squair, J. W. et al. Recovery of walking after paralysis by regenerating characterized neurons to their natural target region. *Science* **381**, 1338–1345 (2023).
17. Skinnider, M. A. et al. Single-cell and spatial atlases of spinal cord injury in the *Tabulae Paralyticae*. *Nature* **631**, 130–163 (2024).
18. Zheng, G. X. Y. et al. Massively parallel digital transcriptional profiling of single cells. *Nat. Commun.* **8**, 14049 (2017).
19. Skinnider, M. A. et al. Cell type prioritization in single-cell data. *Nat. Biotechnol.* **39**, 30–34 (2021).
20. Squair, J. W. et al. Confronting false discoveries in single-cell differential expression. *Nat. Commun.* **12**, 5692 (2021).
21. Squair, J. W., Skinnider, M. A., Gautier, M., Foster, L. J. & Courtine, G. Prioritization of cell types responsive to biological perturbations in single-cell data with Augur. *Nat. Protoc.* **16**, 3836–3873 (2021).
22. Jessell, T. M. Neuronal specification in the spinal cord: inductive signals and transcriptional codes. *Nat. Rev. Genet.* **1**, 20–29 (2000).
23. Azim, E., Jiang, J., Alstermark, B. & Jessell, T. M. Skilled reaching relies on a V2a propriospinal internal copy circuit. *Nature* **508**, 357–363 (2014).
24. Dougherty, K. J. & Kiehn, O. Firing and cellular properties of V2a interneurons in the rodent spinal cord. *J. Neurosci.* **30**, 24–37 (2010).
25. Krenz, N. R. & Weaver, L. C. Sprouting of primary afferent fibers after spinal cord transection in the rat. *Neuroscience* **85**, 443–458 (1998).
26. Weaver, L. C. et al. Autonomic dysreflexia and primary afferent sprouting after clip-compression injury of the rat spinal cord. *J. Neurotrauma* **18**, 1107–1119 (2001).
27. Buch, T. et al. A Cre-inducible diphtheria toxin receptor mediates cell lineage ablation after toxin administration. *Nat. Methods* **2**, 419–426 (2005).
28. Saloman, J. L. et al. Gi-DREADD expression in peripheral nerves produces ligand-dependent analgesia, as well as ligand-independent functional changes in sensory neurons. *J. Neurosci.* **36**, 10769–10781 (2016).
29. Klapoetke, N. C. et al. Independent optical excitation of distinct neural populations. *Nat. Methods* **11**, 338–346 (2014).
30. Fennel, L. E. et al. Targeting cells with single vectors using multiple-feature Boolean logic. *Nat. Methods* **11**, 763–772 (2014).
31. Stuart, T. et al. Comprehensive integration of single-cell data. *Cell* **177**, 1888–1902.e21 (2019).
32. Capogrosso, M. et al. A computational model for epidural electrical stimulation of spinal sensorimotor circuits. *J. Neurosci.* **33**, 19326–19340 (2013).
33. Formento, E. et al. Electrical spinal cord stimulation must preserve proprioception to enable locomotion in humans with spinal cord injury. *Nat. Neurosci.* **21**, 1728–1741 (2018).
34. West, C. R. et al. Association of epidural stimulation with cardiovascular function in an individual with spinal cord injury. *JAMA Neurol.* **75**, 630–632 (2018).
35. Harkema, S. J. et al. Epidural spinal cord stimulation training and sustained recovery of cardiovascular function in individuals with chronic cervical spinal cord injury. *JAMA Neurol.* **75**, 1569–1571 (2018).
36. Harkema, S. J. et al. Normalization of blood pressure with spinal cord epidural stimulation after severe spinal cord injury. *Front. Hum. Neurosci.* **12**, 83 (2018).
37. Darrow, D. et al. Epidural spinal cord stimulation facilitates immediate restoration of dormant motor and autonomic supraspinal pathways after chronic neurologically complete spinal cord injury. *J. Neurotrauma* **36**, 2325–2336 (2019).
38. Nightingale, T. E., Walter, M., Williams, A. M. M., Lam, T. & Krassioukov, A. V. Ergogenic effects of an epidural neuroprosthesis in one individual with spinal cord injury. *Neurology* **92**, 338–340 (2019).
39. Aslan, S. C. et al. Epidural spinal cord stimulation of lumbosacral networks modulates arterial blood pressure in individuals with spinal cord injury-induced cardiovascular deficits. *Front. Physiol.* **9**, 565 (2018).
40. Phillips, A. A. et al. An implantable system to restore hemodynamic stability after spinal cord injury. *Nat. Medicine* <https://doi.org/10.1038/s41591-025-03614-w> (2025).
41. Soriano, J. E. et al. Longitudinal interrogation of sympathetic neural circuits and hemodynamics in preclinical models. *Nat. Protoc.* **18**, 340–373 (2022).
42. Minev, I. R. et al. Biomaterials. Electronic dura mater for long-term multimodal neural interfaces. *Science* **347**, 159–163 (2015).
43. Noreau, L. et al. Development and assessment of a community follow-up questionnaire for the Rick Hansen spinal cord injury registry. *Arch. Phys. Med. Rehabil.* **94**, 1753–1765 (2013).
44. Noreau, L., Noonan, V., Cobb, J., Leblond, J. & Dumont, F. Spinal Cord Injury Community Survey: a national, comprehensive study to portray the lives of Canadians with spinal cord injury. *Top. Spinal Cord Inj. Rehabil.* **20**, 249–264 (2014).
45. Hubli, M., Gee, C. M. & Krassioukov, A. V. Refined assessment of blood pressure instability after spinal cord injury. *Am. J. Hypertens.* **28**, 173–181 (2015).
46. Krassioukov, A., Warburton, D. E., Teasell, R., Eng, J. J. & Spinal Cord Injury Rehabilitation Evidence Research Team. A systematic review of the management of autonomic dysreflexia after spinal cord injury. *Arch. Phys. Med. Rehabil.* **90**, 682–695 (2009).
47. Renier, N. et al. iDISCO: a simple, rapid method to immunolabel large tissue samples for volume imaging. *Cell* **159**, 896–910 (2014).

**Publisher's note** Springer Nature remains neutral with regard to jurisdictional claims in published maps and institutional affiliations.



**Open Access** This article is licensed under a Creative Commons Attribution-NonCommercial-NoDerivatives 4.0 International License, which permits any non-commercial use, sharing, distribution and reproduction in any medium or format, as long as you give appropriate credit to the original author(s) and the source, provide a link to the Creative Commons licence, and indicate if you modified the licensed material. You do not have permission under this licence to share adapted material derived from this article or parts of it. The images or other third party material in this article are included in the article's Creative Commons licence, unless indicated otherwise in a credit line to the material. If material is not included in the article's Creative Commons licence and your intended use is not permitted by statutory regulation or exceeds the permitted use, you will need to obtain permission directly from the copyright holder. To view a copy of this licence, visit <http://creativecommons.org/licenses/by-nc-nd/4.0/>.

© The Author(s) 2025

# Article

## Methods

### Mouse and rat models

Adult male or female C57BL/6 mice (15–25 g body weight, 8–15 weeks of age) or transgenic mice were used for all experiments. vGLUT2-Cre (016963, Jackson Laboratory), Vsx2-Cre (MMMRRC 36672, also called Chx10-Cre), ChAT-Cre, VGAT-Cre, Ai65(RCFL-tdT) (021875; Jackson Laboratory), PV-Cre (017320, Jackson Laboratory), Advillin<sup>Flopo</sup> (a gift from V. Abraira), iDTR and Calca-Cre transgenic mouse strains were bred and maintained on a mixed genetic background (C57BL/6). Adult female Lewis rats (180–220 g body weight, 14–30 weeks of age) were used for the rat experiments. Housing, surgery, behavioural experiments and euthanasia were all performed in compliance with the Swiss Veterinary Law guidelines. Manual bladder voiding and all other animal care was performed twice daily throughout the entire experiment. All procedures and surgeries were approved by the Veterinary Office of the Canton of Geneva (Switzerland; authorization GE67).

### Viral vectors and vector production

Viruses used in this study were either acquired commercially or produced at the EPFL core facility. The following AAV plasmids were used and detailed sequence information is available as detailed or upon request: AAVDJ-hSyn-flex-mGFP-2A-synaptophysin-mRuby<sup>48</sup> (reference AAV DJ GVVC-AAV-100, Stanford Vector Core Facility), AAV9-CMV-Cre (7014, Vector Biolabs), AAV5-hSyn-eGFP (50465-AAV5, Addgene), AAV5-Syn-flex-ChrimsonR-tdT (62723, Addgene), AAV5-hSyn-DIO-hm4D<sup>49</sup> (Gi)-mCherry (44362, Addgene; 7 × 10<sup>12</sup> vg ml<sup>-1</sup> or more), AAV5-CAG-flex-tdTomato (a gift from S. Arber), AAV5-hSyn-Con/Fon-eYFP (#55650, Addgene), rAAV2-EF1a-DIO-Flopo (#87306, Addgene), EnvA-ΔG-Rabies-mCherry (a gift from S. Arber) and AAV8-hSyn-dlox-TVA950-2A-EGFP-2A-oGrev-dlox-WRPE-bGHP (a gift from S. Arber).

### SCI models

For mouse SCIs, a laminectomy was performed on the T4 vertebra to expose the T4 spinal segment. Complete transections were performed using angled microscissors. Rat SCIs were performed according to our previously published work<sup>6</sup>. In brief, a laminectomy was performed on the T3 vertebra to expose the T3 spinal segment. Following this, the rat was transferred to the Infinite Horizon (IH-0400 Impactor, Precision Systems and Instrumentation) impactor<sup>6</sup> stage, where the T2 and T4 spinous processes were securely clamped using modified Allis forceps<sup>6</sup>. The rat was stabilized on the platform and the impactor tip (2.5 mm) was properly aligned using a 3D coordinate system moving platform. The Infinite Horizon system was set to deliver an impact force of 400 kdyn, with a 5-s dwell time<sup>6</sup>. Analgesia (buprenorphine; Essex Chemie; 0.01–0.05 mg kg<sup>-1</sup>, subcutaneously) and antibiotics (amoxicillin 200 mg per 4 ml; Sandoz; 200 mg l<sup>-1</sup> ad libitum) were provided for 3 and 5 days after surgery, respectively. Bladders were manually expressed twice a day until the end of the experiment<sup>50</sup>.

### Rodent anaesthesia use

All non-terminal experiments were conducted by anaesthetizing animals with isoflurane (initial induction at 5% and maintained on a Bain's system at 2%). Terminal haemodynamic assessments were carried out as previously described 4 weeks after SCI. In brief, animals were anaesthetized with urethane (1.5 g kg<sup>-1</sup>, intraperitoneally)<sup>6</sup>. The depth of anaesthesia was continually monitored by assessing withdrawal reflexes and respiratory rate.

### Haemodynamic monitoring

In mice, carotid artery catheterization was performed. After induction of anaesthesia, the hair on the neck of mice was shaved, and the surgical site cleaned with alcohol and betadine. The right common carotid artery was exposed and isolated from the internal jugular vein using

blunt dissection. The rostral portion of the carotid artery immediately below bifurcation was permanently occluded, whereas the caudal portion of the vessel was temporarily occluded using 5-0 silk sutures. A bent-tip 30-gauge needle was used to create a small hole on top of the carotid artery. The blood pressure sensor was inserted into the carotid artery and advanced approximately 0.5 cm caudally. The catheter was then secured with two 5-0 silk sutures. In rats, the procedure for the telemeter implantation was performed according to our previously published work<sup>6</sup>. In brief, we recorded blood pressure using wireless telemeters (TRM56SP SNA and Pressure Telemeter, Kaha Sciences). A midline abdominal incision was made to expose the peritoneal cavity, followed by a blunt dissection to reach the descending aorta. The aorta was temporarily occluded using a 4-0 silk, 1–2 mm rostral to the iliac bifurcation. The pressure sensor was inserted in the aorta so that the tip was just caudal to the renal artery and fixed with a surgical mesh and biocompatible surgical glue.

### Colorectal distension to induce autonomic dysreflexia

Foley Catheter Cysto-Care 1.5 ml and Foley Catheter Cysto-Care 3 ml were used for mice and rats, respectively, to perform colorectal distension to induce autonomic dysreflexia<sup>51</sup>. The catheter was inserted into the rectum and colon until the balloon was no longer exposed. During colorectal distension assessments, the balloon was inflated (up to 0.7 ml for mice and up to 2.5 ml in rats) for 60 s. Subsequent trials were only initiated after blood pressure had returned to the baseline value. For repetitive autonomic dysreflexia experiments, the balloon was inflated for 30 s and deflated for 60 s and this protocol cycled for 90 min (ref. 14).

### EES implants

All the procedures have been previously detailed<sup>6,13,52–56</sup>. To position electrodes to deliver EES in mice, laminotomies (removal of only the connective tissue between the bones, but not the bones) were performed at T9–T10 and T12–T13 to expose the spinal cord. Teflon-coated stainless steel wires connected to a percutaneous connector (Omnetics Connector Corporation) were inserted rostrally and passed between the spinal cord and the vertebral bones to the other opening. A small part of insulation was removed and the exposed stimulation sites were positioned over T12–T13. A common ground was inserted subcutaneously. The percutaneous connector was cemented to the skull. This stimulation protocol was subsequently used for all acute and chronic experiments. In rats, the implantation of the e-dura was performed according to our previously published work<sup>6</sup>. To insert and stabilize e-dura implants into the epidural space, two partial laminectomies were performed at vertebrae levels L1–L2 and T8–T9 to create entry and exit points for the implant. The implant was gently pulled above the dura mater using a surgical suture. Electrophysiological testing was performed intra-operatively to fine-tune positioning of electrodes. The connector of the implant was secured into a protective cage plastered using freshly mixed dental cement on top of the L2–L3 vertebra. Stimulation was then delivered as previously described<sup>6</sup>. The headstage was plastered using freshly mixed dental cement on the dorsal side of the skull where three stainless steel screws were placed.

### Autonomic neurorehabilitation

In mice, we delivered EES with conventional stimulation protocols<sup>6</sup> that involved continuous EES delivered at 50 Hz with 5-ms pulses at 100–150 µA (2100 Isolated Pulse Stimulator, A-M Systems). Mice underwent autonomic neurorehabilitation consisting of EES applied for 30 min each day for 4 weeks, starting 1 week after SCI. In rats, we applied a closed-loop controlled stimulation using a proportional integral controller that adjusts the amplitude of traveling EES waves over the three haemodynamic hotspots (MATLAB). Next, we applied a +10 mmHg systolic blood pressure target from the baseline acquired at the beginning of each autonomic neurorehabilitation session<sup>6</sup>.

Rats received 30 min of closed-loop controlled stimulation for 6 weeks, starting 1 week after SCI.

### Neuron-specific ablations and chemogenetic manipulations

For ablation experiments with the diphtheria toxin, we used PV<sup>Cre</sup>::Avil<sup>FLPo</sup>::iDTR and Calca<sup>Cre</sup>::Avil<sup>FLPo</sup>::iDTR mice. Four weeks after the SCIs (T4 spinal-level complete transection), mice received intraperitoneal injections of diphtheria toxin (D0564, Sigma) diluted in saline (100 µg kg<sup>-1</sup>) to target PV<sup>ON</sup> or Calca<sup>ON</sup> neurons, respectively. Mice were tested 2 weeks post-injection. To manipulate the activity of vGLUT2<sup>ON</sup> and VGAT<sup>ON</sup> neurons, AAV5-hSyn-DIO-hm4D was infused (0.15 µl per injection) at two depths (0.8 mm and 0.4 mm below the dorsal surface) and separated by 1 mm in either the lower thoracic spinal cord (T11–T13) or the lumbosacral spinal cord (L5–S1) of either vGLUT2–Cre or VGAT–Cre mice before performing the SCI. To manipulate ChAT<sup>ON</sup> neuronal activity, AAV5-hSyn-DIO-hm4D was infused (0.15 µl per injection) at two depths (0.8 mm and 0.4 mm below the dorsal surface) and separated by 1 mm in the lower thoracic spinal cord (T11–T13) of ChAT–Cre mice before performing the SCI. To manipulate SC<sup>THORACIC::Vsx2</sup> or SC<sup>LUMBAR::Vsx2</sup> neurons, AAV5-hSyn-DIO-hm4D was infused in either the lower thoracic spinal cord (T11–T13) or the lumbosacral spinal cord (L5–S1; injection depths were 0.8 mm and 0.4 mm below the dorsal surface; separated by 1 mm; 0.15 µl per injection), respectively, in Vsx2–Cre mice before performing the SCI. After 4 weeks, autonomic dysreflexia or EES-induced pressor response was assessed before and between 30 min and 45 min after intraperitoneal injections of 5 mg kg<sup>-1</sup> clozapine N-oxide (Carbo-synth, CAS: 34233-69-7; suspended in 2% DMSO in saline).

### Optogenetic manipulation

To optogenetically manipulate Vsx2<sup>ON</sup> neurons, AAV5-Syn-flex-Chrimson (#62723-AAV5, Addgene; titre  $\geq 5 \times 10^{12}$  vg ml<sup>-1</sup>) was infused in either the lower thoracic spinal cord (T11–T13) and the lumbosacral spinal cord (L5–S1), in Vsx2–Cre mice before performing the SCI. After 6 weeks, laminectomies were made over T11/T12/T13 and L5/L6/S1 spinal segments. Five-ms pulses were delivered at 50 Hz from a 635-nm laser (LRD-0635-PFR-00100-03, LaserGlow Technologies). Laser light was delivered to the surface of the spinal cord through a fibre optic cable attached to 400 µm, 0.39 NA cannula with a 5-mm tip (Thorlabs). Optical power was set to 2.35 mW at the tip.

### Spinal injections for exclusive labelling of Vsx2<sup>ON</sup> neurons

To exclusively label Vsx2<sup>ON</sup> neurons in the lumbosacral spinal cord with long-distance projections to the lower thoracic region (SC<sup>LUMBAR::Vsx2</sup>), we leveraged Boolean logic viral strategies<sup>30</sup>. Partial laminectomies were made over the T11/T12/T13 and L5/L6/S1 spinal segments of Vsx2–Cre mice. Two sets of bilateral injections of AAV5-hSyn-Con/Fon-eYFP (#55650-AAV8, Addgene; titre  $\geq 1 \times 10^{13}$  vg ml<sup>-1</sup>)<sup>30</sup> were made over the L5/L6/S1 spinal segments (0.25 µl per injection) at a depth of 0.6 mm below the dorsal surface and separated by 1 mm. Two sets of bilateral injections of rAAV2-EF1a-DIO-Flpo (#87306, Addgene) were made over the T11/T12/T13 spinal segments (0.15 µl per injection) at two depths (0.8 mm and 0.4 mm below the dorsal surface) and separated by 1 mm. Animals were perfused 4 weeks later. To label lower thoracic Vsx2<sup>ON</sup> neurons (SC<sup>THORACIC::Vsx2</sup>), two sets of bilateral injections of AAV5-CAG-flex-tdtomato were made over T11/T12/T13 spinal levels (0.15 µl per injection) at two depths (0.8 mm and 0.4 mm below the dorsal surface) and separated by 1 mm.

### Spinal injections for exclusive labelling of vGLUT2<sup>ON</sup> neurons

To exclusively label vGLUT2<sup>ON</sup> neurons in the lumbosacral spinal cord with long-distance projections to the lower thoracic region, we leveraged Boolean logic viral strategies<sup>30</sup>. Partial laminectomies were made over the L5/L6/S1 spinal segments of vGLUT2–Cre mice. Two sets of bilateral injections of AAVDJ-hSyn-flex-mGFP-2A-synaptophysin-mRuby<sup>48</sup> (reference AAV DJ GVVC-AAV-100, Stanford Vector Core Facility) were

made over the L5/L6/S1 spinal segments (0.25 µl per injection) at a depth of 0.6 mm below the dorsal surface and separated by 1 mm. Animals were perfused 4 weeks later.

### Injection site quantification

To determine the number of transfected neurons within the injection site of the spinal cord, we implemented the spot detection function in Imaris. Following the semi-automatic detection of transfected neurons within representative sections per animal, we quantified the neurons by compiling the exported text file from Imaris.

### Perfusions

Animals were perfused at the end of the experiments. Animals were deeply anaesthetized by an intraperitoneal injection of 0.2 ml sodium pentobarbital (50 mg ml<sup>-1</sup>). Animals were transcardially perfused with phosphate-buffered saline (PBS) followed by 4% paraformaldehyde (PFA) in PBS. Tissues were removed and post-fixed overnight in 4% PFA before being transferred to PBS or cryoprotected in 30% sucrose in PBS.

### Immunohistochemistry

Immunohistochemistry was performed as previously described<sup>55,57,58</sup>. Perfused post-mortem tissue was cryoprotected in 30% sucrose in PBS for 48 h before being embedded in cryomatrix (Tissue Tek O.C.T., Sakura Finetek Europe B.V.) and freezing. We used two procedures to identify the segment of the spinal cord. First, we identified the dorsal roots in the unsectioned spinal cord. On the basis of the location of the dorsal root entry zones, we prepared well-defined blocks of spinal cord. We then confirmed that the grey matter of the segments possess the expected laminar organization and morphology. Transverse or horizontal sections (30 µm thick) of the spinal cord were cut on a cryostat (Leica), immediately mounted on glass slides and dried or placed in free floating wells containing PBS + 0.03% sodium azide. The sections were incubated with following primary antibody diluted in blocking solution at room temperature overnight: rabbit anti-Fos (1:500), chicken anti-vGLUT1 (1:500), rabbit anti-ChAT (1:100, Sigma-Aldrich) and rabbit anti-Chx10 (now known as Vsx2; 1:500, Synaptic Systems). Fluorescent secondary antibodies were conjugated to Alexa 488 (green), Alexa 405 (blue), Alexa 555 (red) or Alexa 647 (far red; Thermo Fisher Scientific). For the nuclear stain, 4',6-diamidino-2-phenylindole dihydrochloride (DAPI; 2 ng ml<sup>-1</sup>; Molecular Probes). Sections were imaged digitally using a slide scanner (Olympus VS-120 slide scanner) or confocal microscope (LSM880 + Airy fast module with ZEN 2 Black software, Zeiss). Images were digitally processed using ImageJ (ImageJ NIH) software or Imaris (Bitplane, v9.8.2).

### Fluorescence in situ hybridization

We performed in situ hybridization of cell-type markers and using RNAscope (Advanced Cell Diagnostics). Lists of putative marker genes were obtained from snRNA-seq data, as described below, and cross-referenced against a list of validated probes designed and provided by Advanced Cell Diagnostics. Probes were obtained for the following genes: ChAT (catalogue no. 408731) and Vsx2 (catalogue no. 438341), Slc17a6 (catalogue no. 319171) and Slc6a5, catalogue no. 409741. We then generated 12-µm cryosections from fixed-frozen spinal cords as previously described<sup>59</sup> and performed FISH for each probe according to the manufacturer's instructions, using the RNAscope HiPlex kit (cat no. 324106). Images were generated using QuPath (v0.4.3).

### iDISCO+

Mice underwent a 90-min colorectal distension protocol (30 s inflate then 60 s deflate repeatedly)<sup>14</sup> and were perfused<sup>49,47</sup> 30 min later with 0.1 M PBS followed by 4% PFA (in 0.1 M PBS). Spinal cords were dissected and post-fixed in 4% PFA (in 0.1 M PBS) at 4 °C overnight and placed in 0.1 M PBS containing 0.03% sodium azide. Immunolabelling of the samples was performed by first pretreating with methanol in

# Article

5-ml Eppendorf tubes by dehydrating with a methanol–H<sub>2</sub>O series at 1 h each at room temperature with shaking at 60 rpm: 20%, 40%, 60%, 80% and 100%. This procedure was followed by 1 h washing with 100% methanol before chilling the samples at 4 °C. Samples were then incubated overnight with shaking in 66% dichloromethane–33% methanol at room temperature. The samples were washed twice in 100% methanol with shaking at room temperature and then bleached in chilled fresh 5% H<sub>2</sub>O<sub>2</sub> in methanol overnight at 4 °C. Samples were rehydrated with a methanol–H<sub>2</sub>O series: 80%, 60%, 40%, 20% and 0.1 M PBS, each for 1 h at room temperature under shaking. Samples were washed for 1 h × 2 at room temperature in PTx.2 buffer (0.1 M PBS with 0.2% Triton X-100) under shaking. This was followed by an incubation in 5 ml of permeabilization solution (400 ml PTx.2, 11.5 g glycine and 100 ml DMSO for a total stock volume of 500 ml) for 2 days at 37 °C with shaking at 60 rpm. Samples were incubated in 5 ml of blocking solution (42 ml PTx.2, 3 ml of normal donkey serum and 5 ml of DMSO for a total stock volume of 50 ml) for 2 days at 37 °C with shaking. The samples were incubated for 7 days at 37 °C with shaking in primary antibody solution consisting of PTwH (0.1 M PBS, 2 ml Tween-20, 10 mg l<sup>-1</sup> heparin, 5% dimethyl sulfoxide and 3% normal donkey serum) and Fos antibody (1:2,000; 226003, Synaptic Systems) for a total volume of 5 ml per sample. Samples were washed in PTwH for 24 h with shaking and incubated for 7 days at 37 °C with shaking in secondary antibody solution consisting of PTwH, 3% normal donkey serum and donkey anti-rabbit Alexa Fluor 647 (1:400, Thermo Fisher Scientific) in a total volume of 5 ml per sample. Samples were washed in PTwH for 24 h with shaking at room temperature. Clearing of the samples was performed by first dehydrating the samples in a methanol–H<sub>2</sub>O series as follows: 20%, 40%, 60%, 80% and 100% twice each for 1 h with shaking at room temperature followed by a 3-h incubation with shaking in 66% dichloromethane–33% methanol at room temperature. Samples were incubated in 100% dichloromethane 15 min twice with shaking to wash residual methanol. Finally, samples were incubated in 100% dibenzyl ether without shaking for refractive index matching of the solution for at least 24 h before imaging.

## Tissue clearing (CLARITY)

We incubated samples in X-CLARITY hydrogel solution (Logos Biosystems) for 24 h at 4 °C with gentle shaking<sup>12,55,60</sup>. Samples were degassed and polymerized using the X-CLARITY Polymerization System (Logos Biosystems), followed by washes in 0.001 M PBS for 5 min at room temperature. Samples were next placed in the X-CLARITY Tissue Clearing System (Logos Biosystems), set to 1.5 A at 100 rpm at 37 °C for 29 h. Clearing solution was made in-house with 4% sodium dodecyl sulfate, 200 mM boric acid with dH<sub>2</sub>O, pH adjusted to 8.5. Following this, samples were washed for at least 24 h at room temperature with gentle shaking in 0.1 M PBS solution containing 0.1% Triton X-100 to remove excess sodium dodecyl sulfate. Finally, samples were incubated in 40 g of Histodenz dissolved in 30 ml of 0.02 MPB, pH 7.5, and 0.01% sodium azide (refractive index of 1.465) for at least 24 h at room temperature with gentle shaking before imaging.

## 3D imaging

We performed imaging of cleared tissue using either a customized mesoSPIM<sup>12,61</sup> or a CLARITY-optimized light-sheet microscope (COLM)<sup>12</sup>. A custom-built sample holder was used to secure the central nervous system in a chamber filled with RIMS. Samples were imaged using either a ×1.25 or ×2.5 objective at the mesoSPIM<sup>12,61</sup> or a ×4 or ×10 objective at the COLM<sup>12</sup> with one or two light sheets illuminating the sample from both the left and the right sides. The voxel resolution in the x, y and z directions was 5.3 μm × 5.3 μm × 5 μm for the ×1.25 acquisition and 2.6 μm × 2.6 μm × 3 μm for the ×2.5 acquisition. The voxel resolution of the COLM was 1.4 μm × 1.4 μm × 5 μm for the ×4 and 0.59 μm × 0.59 μm × 3 μm for the ×10 acquisition. Images were generated as 16-bit TIFF files and then stitched using Arivis Vision4D

(Arivis AG). 3D reconstructions and optical sections of raw images were generated using Imaris (bitplane, v9.8.2) software.

## Fos quantifications

For the cleared spinal cords, Fos-positive neurons of cleared samples were quantified using Arivis Vision4D (Arivis)<sup>13</sup>. After defining a region of interest around the grey matter, each sample was subjected to a custom-made pipeline. We applied morphology, denoising and normalization filters to enhance the signal of bright objects and homogenized the background. Threshold-based segmentation of the Fos signal was applied within predefined 3D regions to quantify the total number of Fos-positive cells. Image analysis parameters were kept constant among all samples. The number of Fos-positive cells and their coordinates enabled us to quantify the neuronal activity segment by segment. For the classic immunohistochemistry, the quantification was done on Imaris (bitplane, v9.8.2) using the spot detection function.

## 3D reconstruction and quantification

We used the ‘add new surfaces’ tool in Imaris to select the channel of interest, setting the ‘surface detail’ to 0.5 μm for a more detailed surface. The ‘threshold (absolute intensity)’ was adjusted to capture the full shape of the neuron accurately. We applied the ‘number of voxels Img = 1’ filter, selecting the appropriate threshold values to include the reconstructed neuron. After rendering the surface, we made aesthetic adjustments, choosing the ‘transparent 3 - glass’ material and setting the colour to RGB values of (1, 1, 1) to maintain transparency and highlight viral expression. For reconstructing synaptic-like appositions, we created ‘spots’ based on the channel of interest using the spot detection algorithm in Imaris. The ‘estimate xy diameter’ was set between 1.5 μm and 2 μm, with the ‘quality’ filter applied to capture all synaptic-like appositions in the image. The ‘points style/quality’ was set to ‘sphere’ with a ‘radius scale’ of 0.5 μm, using ‘Phong\_basic’ as the material for the synapses. To filter synaptic-like appositions to neurons of interest, we used the ‘find spots close to surface’ function with a 1-μm threshold and selected only the ‘spots close to the surfaces’ to display the synaptic-like appositions on neurons of interest. Of note, synapses were primarily counted on neuronal cell bodies as labelling of the different axonodendritic compartments with *in vivo* immunohistochemistry remains limited.

## Axon and synapse quantification

To determine spatial enrichment of axon and synapse density within the grey horn of the spinal cord, we implemented a custom image analysis pipeline that includes preprocessing, registration and combination of histological images from different animals. In brief, we implemented all preprocessing in Fiji, and all registration procedures in R, using the image analysis package ‘imageR’ and the medical image registration package ‘RNiftyReg’. After dynamic registration, all data were summarized and final quantifications were completed using custom R scripts.

## Opto-tagging-based neuron-specific recordings and analysis

SCI at T4 and infusion of AAV5-Syn-flex-Chrimson was made in the lower thoracic spinal cord of Vsx2-Cre mice at least 4 weeks before terminal experiments. Mice were anaesthetized with urethane and isofluorane. Two-shank, multi-site electrode arrays (A2x32-6mm-35-200-177, NeuroNexus) were lowered into the spinal cord to a depth of 1,000 μm, with shanks arranged longitudinally at 350 μm from the midline. Signals were recorded with a NeuroNexus Smartbox Pro using a common average reference and while applying 50-Hz notch and 450–5,000-Hz bandpass filters. Stimulation was controlled with a Multi-Channel Systems STG 4004 and MC\_Stimulus II software. ChrimsonR-expressing neurons were identified using optogenetic stimulation. Twenty pulse trains of 10-ms pulses were delivered at 10 Hz from a 635-nm laser (LRD-0635-PFR-00100-03, LaserGlow Technologies). Laser light was delivered to the surface of the spinal cord through

a fibre optic cable attached to 400 µm, 0.39 NA cannula with a 5-mm tip (Thorlabs). Optical power was set to 2.35 mW at the tip. Electrical stimulation (EES) consisted of 5-ms pulses delivered every 1 Hz. EES was delivered with a micro fork probe (Inomed, 45 mm straight, item no. 522610) positioned along the midline just caudal to the recording array. Spike sorting was performed with SpyKING CIRCUS (v1.0.773). The median-based average electrical stimulation artefacts for each channel were subtracted from the recordings before sorting. Owing to the size and variability of the artefacts, periods containing residual stimulation artefacts were not sorted ( $-0.5$  to  $+1.5$  ms and  $-0.5$  to  $+1$  ms around stimulus onset for EES and laser stimulation onset, respectively). Sorting results were manually curated using Phy (<https://github.com/cortex-lab/phy>). Single-unit clusters were selected for analysis based on their biphasic waveforms and template amplitudes above 50 µV, as well as strong refractory period dips in their spike autocorrelograms. Similar clusters were merged according to the Phy manual clustering guide. CrimsonR-expressing, putative SC<sup>THORACIC::Vsx2</sup> neurons were identified based on their low-latency and low-jitter responses to light pulses. Neurons responding to EES or tail pinch were identified by a one-sided Wilcoxon signed-rank test to compare the instantaneous firing rate of units 100 ms before and 100 ms after (EES) or 2 s before and 2 s after (pinch) stimulus onset. For EES, a post-stimulus onset firing rate increase of  $P < 0.001$  was used, whereas for pinch a  $P = 0.05$  was used due to the necessarily lower number of trials and larger calculation window (minimum of 6 trials for pinch and 60 trials for EES).

**Statistics, power calculations, group sizes and reproducibility**  
All data are reported as mean values and individual data points. No statistical methods were used to predetermine sample sizes, but our sample sizes are similar to those reported in previous publications<sup>55</sup>. Haemodynamic assays were replicated three to five times, depending on the experiment, and averaged per animal. For all photomicrographs of histological tissue, staining experiments were repeated independently with tissue from at least four, and in most cases six, different animals with similar results. Statistics were then performed over the mean of animals. All statistical analysis was performed in R using the base package ‘stats’, with primary implementation through the ‘tidyverse’ and ‘broom’ packages. Tests used included one-tailed or two-tailed paired or independent samples Student’s *t*-tests, one-way analysis of variance (ANOVA) for neuromorphological evaluations with more than two groups, and one-way or two-way repeated-measures ANOVA for haemodynamic assessments, when data were distributed normally, tested using a Shapiro–Wilk test. Post-hoc Tukey tests were applied when appropriate. For regressions, mixed-model linear regression was used in cases of multiple observations, or else standard linear modelling. In cases where group size was equal to or less than three, null hypothesis testing was not completed. The significance level was set as  $P < 0.05$ . Throughout the paper, the boxplots show the median (horizontal line), interquartile range (hinges) and smallest and largest values no more than 1.5 times the interquartile range (whiskers). Exclusions of data are noted in the relevant Methods sections. Unless stated otherwise, experiments were not randomized, and the investigators were not blinded to allocation during experiments and outcome assessment.

#### scRNA-seq

Single-nucleus dissociation of the mouse lower thoracic and lumbosacral spinal segments was performed according to our established procedures<sup>19,20</sup>. Following euthanasia by isoflurane inhalation and cervical dislocation, the lumbar spinal cord site was immediately dissected and frozen on dry ice. Spinal cords were doused in 500 µl sucrose buffer (0.32 M sucrose, 10 mM HEPES (pH 8.0), 5 mM CaCl<sub>2</sub>, 3 mM Mg acetate, 0.1 mM EDTA and 1 mM dithiothreitol) and 0.1% Triton X-100 with the Kontes Dounce tissue grinder. Sucrose buffer (2 ml) was then added and filtered through a 40-µm cell strainer. The lysate was centrifuged at 3,200g for 10 min at 4 °C. The supernatant was then decanted, and 3 ml

of sucrose buffer was added to the pellet for 1 min. We homogenized the pellet using an Ultra-Turrax and 12.5 ml of density buffer (1 M sucrose, 10 mM HEPES (pH 8.0), 3 mM Mg acetate and 1 mM dithiothreitol) was added below the nuclei layer. The tube was centrifuged at 3,200g at 4 °C and the supernatant poured off. Nuclei on the bottom half of the tube wall were collected with 100 µl PBS with 0.04% BSA and 0.2 U µl<sup>-1</sup> RNase inhibitor. Finally, we resuspended nuclei through a 30-µm strainer and adjusted to 1,000 nuclei per microlitre.

#### Library preparation

snRNA-seq library preparation was carried out using the 10X Genomics Chromium Single Cell Kit (v3.1). The nuclei suspension was added to the Chromium RT mix to achieve loading numbers of 2,000–5,000. For downstream cDNA synthesis (13 PCR cycles), library preparation and sequencing, the manufacturer’s instructions were followed.

#### Read alignment

We aligned reads to the most recent Ensembl release (GRCm38.93) using Cell Ranger, and obtained a matrix of unique molecular identifier (UMI) counts. Seurat<sup>31</sup> was used to calculate quality control metrics for each cell barcode, including the number of genes detected, number of UMIs and proportion of reads aligned to mitochondrial genes. Low-quality cells were filtered by removing cells expressing less than 200 genes or with more than 5% mitochondrial reads. Genes expressed in less than three cells were likewise removed.

#### Clustering and integration

Before clustering analysis, we first performed batch-effect correction and data integration across the two different experimental conditions as previously described<sup>31</sup>. Gene expression data were normalized using regularized negative binomial models<sup>62</sup>, then integrated across batches using the data integration workflow within Seurat. The normalized and integrated gene expression matrices were then subjected to clustering to identify cell types in the integrated dataset, again using the default Seurat workflow. Cell types were manually annotated on the basis of marker gene expression, guided by previous studies of the mouse spinal cord<sup>19,63–65</sup>. Local and projecting neuronal subpopulations were annotated on the basis of *Nfib* and *Zfhx3* expression, respectively<sup>15</sup>. Following our projection-specific snRNA-seq experiment in uninjured mice, each subsequent experiment was reintegrated with this dataset before subpopulation annotation. This enabled the identification of the same 28 neuronal subpopulations across the three distinct experiments<sup>31</sup>.

#### Cell-type prioritization with Augur

To identify neuronal subpopulations perturbed during natural repair, we implemented our machine-learning method Augur<sup>19,21</sup>. Augur was run with default parameters for all comparisons. To evaluate the robustness of cell-type prioritizations to the resolution at which neuronal subtypes were defined in the snRNA-seq data, we applied Augur at various clustering resolutions and visualized the resulting cell-type prioritizations both on a hierarchical clustering tree<sup>66</sup> of neuron subtypes and as a progression of UMAPs. The key assumption underlying Augur is that cell types undergoing a profound response to a perturbation should become more separable, within the highly multidimensional space of gene expression, than less affected cell types. In brief, Augur withhold a proportion of sample labels, then trains a random forest classifier to predict the condition from which each cell was obtained. The accuracy with which this prediction can be made from single-cell gene expression measurements is then evaluated in cross-validation and quantified using the area under the receiver operating characteristic curve.

#### Clinical studies design and objectives

All experiments were carried out as part of three clinical safety (primary objective) and preliminary efficacy (secondary objectives) trials: STIMO-HEMO (NCT04994886, CHUV, Lausanne, Switzerland), HEMO

# Article

(NCT05044923, University of Calgary, Calgary, Canada) and HemON (NCT0511093, CHUV, Lausanne, Switzerland). All three trials and subsequent amendments received approval by the local ethical committees and national competent authorities. All participants signed a written informed consent before their participation, which included consent to complete the autonomic dysreflexia component of the ADFSCI. All participants had the option to indicate consent for the publication of identifiable images or videos. All surgical and experimental procedures were performed at the investigational hospital sites (Neurosurgery Department of the Lausanne University Hospital (CHUV) and the Neurosurgery Department of the Foothills Medical Center (Calgary, Canada). The study involved eligibility and baseline assessments before surgery, the surgical implantation of the respective investigational devices, a post-operative period during which EES protocols were configured, and long-term follow-up periods. To date, a total of ten participants have been participating for more than 6 months in the study. More detailed information about these trials can be found in other publications<sup>40</sup>.

## Study participants

Eleven individuals (five women and six men) who had suffered a traumatic SCI participated overall in the four studies. Demographic data and neurological status, evaluated according to the International Standards for Neurological Classification of Spinal Cord Injury<sup>1</sup>, can be found in Supplementary Table 3.

## Neurosurgical intervention

The participant was put under general anaesthesia and was placed in a prone position. Preoperative surgical planning informed the neurosurgeon about the vertebral entry level and predicted optimal position. On the basis of this knowledge, lateral and anteroposterior fluoroscopy X-rays were performed intraoperatively to guide the location of the laminotomies. A midline skin incision of approximately 5 cm on the back was performed, the fascia opened and the muscles were retracted bilaterally. Excision of the midline ligamentous structures and a laminotomy at the desired entry level enabled the insertion of the paddle array at the spinal thoracic level. For participants of the STIMO-HEMO and HEMO trials, a second skin incision or extended opening caudally was made and a second laminotomy was performed in the lumbar area based on the pre-operative planning to allow for the insertion of the lumbar paddle lead. The paddle lead (or leads; Specify 5-6-5, Medtronic or ARC<sup>TM</sup> Thoracic Lead, ONWARD Medical N.V) were inserted and placed over the midline of the exposed dura mater and advanced rostrally to the target position guided by repeated fluoroscopies. Electrophysiological recordings were conducted using standard neuromonitoring systems (IOMAX, Cadwell Industries or ISIS Xpress, Inomed Medizintechnik). Single pulses of EES (0.5 Hz) were delivered at increasing amplitude to elicit muscle responses that are recorded from the subdermal (Neuroline Twisted Pair Subdermal, 12 × 0.4 mm, Ambu A/S) or intramuscular (Inomed SDN electrodes, 40 × 0.45 mm, Inomed Medizintechnik) needle electrodes to correct for lateral and rostrocaudal positioning. If the paddles were deviating from a straight midline position, small additional laminotomies were made to remove bony protrusions and guide the paddle to a midline placement. Once the final position was achieved, the leads were anchored to the muscular fascia. In the STIMO-HEMO and HemON trials, the back opening was temporarily closed and the participant was put in lateral decubitus. Subsequently, the back incision was reopened and an abdominal incision of about 5 cm was made per implantable pulse generator (IPG) and a subcutaneous pocket was created. In the HEMO trial, incisions of about 5 cm were made bilaterally in the upper buttocks region and subcutaneous pockets were created. The paddle array cables were then tunneled between the back opening and subcutaneous pockets to be connected to the IPGs (Intellis, Medtronic or ARC<sup>TM</sup> IPG, ONWARD Medical). The IPGs were implanted in the subcutaneous pockets and all incisions were finally closed.

## Stimulation optimization

Spatial mapping was guided by the preclinical mechanisms previously described<sup>6</sup> and from previous clinical mappings<sup>40</sup>, and was conducted in three steps: (1) intra-operative mapping to identify which rows of electrodes target the haemodynamic hotspot, and elicit the largest pressor response in the thoracic spinal cord (T10, T11 and T12), (2) post-operative imaging and spinal reconstructions were used to estimate the electrodes that maximize recruitment of the haemodynamic hotspots, and (3) a single 2-h, post-operative mapping session was done to test each row of electrodes on the lead and pick the three configurations with the largest pressor responses. These configurations were tested in both multipolar and monopolar settings and were validated by personalized simulations to ensure that we were optimally targeting the haemodynamic hotspots. Stimulation frequency was defined empirically at 120 Hz for the spatial mapping<sup>6,40</sup>. The pulse width was 300 µs. The amplitude was set by incrementally increasing the current per configuration until the systolic pressure increased by 20 mmHg, the diastolic pressure increased by 10 mmHg, or the patient did not report any discomfort such as muscle contractions or sensations such as tingling. These mappings were done in a seated position to mimic relevant, daily life orthostatic challenges.

## Clinical haemodynamic monitoring

Beat-to-beat blood pressure and heart rate were obtained via finger plethysmography (Finometer, Finapres Medical Systems). Beat-by-beat blood pressure was calibrated to brachial artery blood pressure collected using an arm cuff embedded and synchronized with the Finometer<sup>67–70</sup>. Brachial arterial pressure was sampled at 200 Hz, whereas the systolic, diastolic and mean arterial pressures were extracted from the calibrated arterial pressure at 1 Hz. The heart rate was also sampled at 1 Hz. Raw data and automatically extracted haemodynamic parameters were saved and exported from the Finometer.

## Orthostatic challenge with the tilt table test

Participants were transferred to a supine position on a table capable of head-up tilt. We applied restraint straps to secure the patient below the knees, across the thighs and the trunk, with the feet stabilized. Resting supine blood pressure was recorded continuously for approximately 5–10 min to establish baseline values. Then, we tilted the patient upright up to a maximum of 70° while recording haemodynamic values and symptoms of orthostatic tolerance. The time to reach the desired tilt angle from supine was achieved in less than 45 s. Participants were tilted until reaching their tolerance threshold or for a maximum duration of 10 min. They were asked not to talk during the test except to inform and grade symptoms. The participant was asked to report any symptoms every 1–3 min. The participant was asked to rank their symptoms between 1–10, 1 being no symptoms at all, and 10 being feelings of dizziness, lightheadedness<sup>71</sup> or nausea<sup>37,71</sup>. The patient was instructed to notify the research team if they needed to be returned to the supine position.

## Post-operative blood pressure data

During a tilt test (see the section ‘Orthostatic challenge with the tilt table test’), changes in blood pressure were recorded without stimulation or in response to different types of stimulation (continuous or closed-loop stimulation) using the Finometer (see the section ‘Clinical haemodynamic monitoring’). Change in blood pressure or heart rate was defined as the difference in the average of a 60-s window before the start of the tilt and a 20-s window at 3 min of the challenge. If the participant could not tolerate at least 3 min of the test due to low blood pressure or other symptoms, an average of a 20-s window before the end of the tilt was used. All measurements in seated position were measured with stimulation on for 3–5 min. Change in blood pressure, or heart rate, was defined as the difference in the average of a 20-s window before the

start of EES and the average of a 20-s window at 3 min, before stopping stimulation. All signals were smoothed over a 10-s window for illustration. The same processing was used for post-operative, day 1 quantification. In the present study, we report on blood pressure data on the two study participants implanted with the full ARC<sup>TM</sup> implantable system.

### Off-label investigational system

The investigational system used in the STIMO-HEMO and HEMO clinical trials consisted of a set of CE-marked, FDA-approved medical devices used off-label. Two IPGs (Intellis with AdaptiveStim, Medtronic) are connected to their respective paddle leads (Specify 5-6-5 SureScan MRI, Medtronic), both indicated for chronic pain management. A tablet application with a communicator device (Intellis clinician programmer, Medtronic) was used by the clinical team to wirelessly set up the system and optimize the stimulation parameters. A remote control device and transcutaneous charger device (Patient Programmer and Recharger, Medtronic) were used by the participants to charge the IPGs and wirelessly turn the stimulation on and off during daily life and adapt a subset of stimulation parameters defined by the clinical team.

### Purpose-built investigational system for restoring haemodynamic stability

The investigational system used in the HemON was purpose-built for restoring haemodynamic stability. A step-wise approach was followed. All participants were implanted with a purpose-built IPG (ARC<sup>TM</sup> Thoracic System, ONWARD Medical) that communicates with a purpose-built ecosystem of control devices. The first four participants of the HemON clinical trial received an off-label paddle lead (Specify 5-6-5 SureScan MRI, Medtronic), whereas all other participants were implanted with a novel, purpose-built, paddle lead (ARC<sup>TM</sup> Thoracic Lead, ONWARD Medical).

### Purpose-built IPG and communication ecosystem for restoring haemodynamic stability

The purpose-built ARC<sup>TM</sup> IPG developed by ONWARD Medical is a novel 16-channel IPG developed to deliver targeted EES. It controls and delivers current-controlled stimulation pulses according to predefined stimulation programmes or through commands received in real time to monopolar or multipolar electrode configurations on 16 channels. The IPG consists of a hermetically sealed, biocompatible can that surrounds the electrical components and a rechargeable battery that enables its function. The IPG is composed of two main components: the header containing the connector block that enables connection with two eight-contact lead connectors as well as two coils for charging and communication, and the can with a rechargeable battery and electronics circuits. The IPG was developed according to all applicable standards for medical device development. Conventional biomedical technologies were used to fabricate the IPG and extensive bench, and *in vivo* testing was performed to verify its performance. The IPG was implanted subcutaneously at the abdominal level and communicates wirelessly with the ARC<sup>TM</sup> Hub with near-field magnetic induction. This wearable device was worn on a belt over or in proximity to the IPG location and was responsible for wirelessly charging the IPG's battery and for programming the IPG with stimulation settings received from several user interfaces. The communication between the hub and IPG provides real-time control of stimulation parameters (as fast as approximately 25 ms between command and stimulation execution), allowing integration with a fast closed-loop neuromodulation system. The ARC<sup>TM</sup> Hub contains a Bluetooth low-energy chip to enable fast, reliable wireless communication with external programmers such as the ARC<sup>TM</sup> Clinician Programmer, an Android app designed for clinicians to configure and test the implanted system and personalized stimulation programs. When a stimulation program was deemed safe for personal use, the Clinician Programmer can be used to make this stimulation program available to the patient. The patients, or their caregivers,

can control the system through the ARC<sup>TM</sup> Personal Programmer. This Android watch application allows users to select, start and stop stimulation programs, as well as modulate stimulation amplitudes within predefined safety limits ad hoc. Device errors, paddle lead impedances and daily stimulation utilization were extracted from usage logs across all devices. Furthermore, the Clinician Programmer includes an application programming interface (the ARC<sup>TM</sup> API) that enables other programming softwares to control the stimulation, for example, for closed-loop control of the stimulation. All devices and softwares are adherent to the applicable standards and their performance was extensively tested. The entire system, including the IPG, received the equivalent of an investigational device exemption from the competent Swiss authorities.

### Purpose-built paddle lead

The ARC-IM Thoracic Lead developed by ONWARD Medical is a new 16-electrode paddle lead that is designed for selective recruitment of the dorsal root entry zones of the low-thoracic spinal cord with optimal coverage of the T10–T12 spinal levels. More detailed information about this paddle lead can be found in other publications<sup>40</sup>.

### SCI community survey

Ethical approval was obtained from an independent ethics board (Veritas Independent Review Board) and the Research Ethics Board of Université Laval (principal investigator's institution). Ethical approval from local research ethics boards was also obtained to recruit from SCI centres across Canada. Individuals with SCI ( $n = 1,479$ ) across Canada were recruited using a national consumer awareness campaign and provided written informed consent<sup>43,44</sup>. The survey consisted of a series of variables identified by health-care and service providers, researchers and individuals with SCI, including demographics, secondary health complications, comorbidities, SCI-related needs, health-care utilization, community participation, quality of life and overall health ratings<sup>43,44</sup>. Participants were asked how often they had experienced symptoms of autonomic dysreflexia in the past 12 months and responses were ranked on a six-point ordinal severity scale ranging from 0 ('never') to 5 ('every day'). Participants were also asked whether they received or sought out treatment concerning these symptoms on a two-point scale ('yes' or 'no'), along with the degree to which it limited activities from 0 ('never') to 5 ('every day'). Participants were also asked whether they had experienced specific problems, such as heart disease, in the past 12 months. Participants' American Spinal Injury Association Impairment Scale was estimated using responses to questions about lesion level and sensorimotor and/or mobility capabilities. A binary approach was used for the evaluation of outcome variables including the level of injury (cervical SCI versus non-cervical SCI), the severity of injury (complete versus incomplete), the presence of autonomic dysreflexia (yes versus no) and autonomic dysreflexia symptoms (yes versus no). For variables ranked on a six-point ordinal scale, lower scores (0–3) were categorized as 'no' and higher scores (4–5) were categorized as 'yes'.

### ADFSCL

The ADFSCI is a 24-item questionnaire divided into four sections: demographics, medication, autonomic dysreflexia and orthostatic hypotension. The autonomic dysreflexia section consists of seven items. Each item used a five-point scale to measure the frequency and severity of symptoms related to autonomic dysreflexia, including headaches, goosebumps, heart palpitations, sweating and anxiety, across different situational contexts. Participants were categorized as experiencing symptoms if the item score was higher than 2 or not experiencing symptoms otherwise. For data collection related to the ADFSCI of individuals not involved in the ongoing clinical studies, Conjoint Health Research Ethics Board approval (REB21-0045) was obtained from the University of Calgary. All participants provided written informed consent before providing their responses.

**Reporting summary**

Further information on research design is available in the Nature Portfolio Reporting Summary linked to this article.

**Data availability**

Data that support the findings and software routines developed for the data analysis will be made available on reasonable request to the corresponding authors. Source data are provided with this paper. Raw sequencing data and count matrices have been deposited to the Gene Expression Omnibus (GSE256423).

**Code availability**

Augur is available on GitHub (<https://github.com/neurorestore/Augur>).

48. Grimm, D. et al. In vitro and in vivo gene therapy vector evolution via multispecies interbreeding and retargeting of adeno-associated viruses. *J. Virol.* **82**, 5887–5911 (2008).
49. Armbruster, B. N., Li, X., Pausch, M. H., Herlitze, S. & Roth, B. L. Evolving the lock to fit the key to create a family of G protein-coupled receptors potently activated by an inert ligand. *Proc. Natl Acad. Sci. USA* **104**, 5163–5168 (2007).
50. Ramsey, J. B. G. et al. Care of rats with complete high-thoracic spinal cord injury. *J. Neurotrauma* **27**, 1709–1722 (2010).
51. Zhang, Y. et al. Autonomic dysreflexia causes chronic immune suppression after spinal cord injury. *J. Neurosci.* **33**, 12970–12981 (2013).
52. Wenger, N. et al. Spatiotemporal neuromodulation therapies engaging muscle synergies improve motor control after spinal cord injury. *Nat. Med.* **22**, 138–145 (2016).
53. Courtine, G. et al. Transformation of nonfunctional spinal circuits into functional states after the loss of brain input. *Nat. Neurosci.* **12**, 1333–1342 (2009).
54. Brand, R. v. d. et al. Restoring voluntary control of locomotion after paralyzing spinal cord injury. *Science* **336**, 1182–1185 (2012).
55. Asboth, L. et al. Cortico-reticulo-spinal circuit reorganization enables functional recovery after severe spinal cord contusion. *Nat. Neurosci.* **21**, 576–588 (2018).
56. Capogrosso, M. et al. Configuration of electrical spinal cord stimulation through real-time processing of gait kinematics. *Nat. Protoc.* **13**, 2031–2061 (2018).
57. Anderson, M. A. et al. Required growth facilitators propel axon regeneration across complete spinal cord injury. *Nature* **561**, 396–400 (2018).
58. Anderson, M. A. et al. Astrocyte scar formation aids central nervous system axon regeneration. *Nature* **532**, 195–200 (2016).
59. Wang, F. et al. RNAscope: a novel in situ RNA analysis platform for formalin-fixed, paraffin-embedded tissues. *J. Mol. Diagn.* **14**, 22–29 (2012).
60. Chung, K. et al. Structural and molecular interrogation of intact biological systems. *Nature* **497**, 332–337 (2013).
61. Voigt, F. F. et al. The mesoSPIM initiative: open-source light-sheet microscopes for imaging cleared tissue. *Nat. Methods* **16**, 1105–1108 (2019).
62. Hafermeister, C. & Satija, R. Normalization and variance stabilization of single-cell RNA-seq data using regularized negative binomial regression. *Genome Biol.* **20**, 296 (2019).
63. Zeisel, A. et al. Molecular architecture of the mouse nervous system. *Cell* **174**, 999–1014.e22 (2018).
64. Häring, M. et al. Neuronal atlas of the dorsal horn defines its architecture and links sensory input to transcriptional cell types. *Nat. Neurosci.* **21**, 869–880 (2018).
65. Sathyamurthy, A. et al. Massively parallel single nucleus transcriptional profiling defines spinal cord neurons and their activity during behavior. *Cell Rep.* **22**, 2216–2225 (2018).
66. Zappia, L. & Oshlack, A. Clustering trees: a visualization for evaluating clusterings at multiple resolutions. *Gigascience* **7**, giy083 (2018).

67. Bogert, L. W. J. & van Lieshout, J. J. Non-invasive pulsatile arterial pressure and stroke volume changes from the human finger. *Exp. Physiol.* **90**, 437–446 (2005).
68. Jansen, J. R. et al. A comparison of cardiac output derived from the arterial pressure wave against thermodilution in cardiac surgery patients. *Br. J. Anaesth.* **87**, 212–222 (2001).
69. Westerhof, B. E., Gisolf, J., Stok, W. J., Wesseling, K. H. & Karemker, J. M. Time-domain cross-correlation baroreflex sensitivity: performance on the EUROBAVAR data set. *J. Hypertens.* **22**, 1371–1380 (2004).
70. Whinnett, Z. I. et al. Multicenter randomized controlled crossover trial comparing hemodynamic optimization against echocardiographic optimization of AV and VV delay of cardiac resynchronization therapy: the BRAVO trial. *JACC Cardiovasc. Imaging* **12**, 1407–1416 (2019).
71. Phillips, A. A., Krassioukov, A. V., Ainslie, P. N. & Warburton, D. E. R. Perturbed and spontaneous regional cerebral blood flow responses to changes in blood pressure after high-level spinal cord injury: the effect of midodrine. *J. Appl. Physiol.* **116**, 645–653 (2014).

**Acknowledgements** This work was financially supported by: Eurostars project E113969 PREP2GO; DARPA subaward A21-0795-S001 (P.O. 1083297); the Office of the Assistant Secretary of Defense for Health Affairs through the Spinal Cord Injury Research Program (HT9425-23-1-0547); Eurostars E1748 IMPULSE; Medtronic (ERP-2020-12543); Onward Medical, PHRT-279; University of Calgary Research Excellence Chair; Brain Canada; Digital Research Alliance of Canada; the Natural Sciences and Engineering Research Council of Canada; the Canadian Institutes of Health Research; Alberta Innovates Health Solutions; Campus Alberta Neuroscience; the Libin Cardiovascular Institute; the Hotchkiss Brain Institute; the Hopewell M.I.N.D. Prize; the Krembil Research Institute; the McCaig Institute for Bone and Joint Health; ONWARD Medical; the Swiss National Science Foundation (the National Centre of Competence in Research in Robotics, 5INF40\_185543); Canadian Institutes of Health Research (Graduate Scholarship), the Branch Out Neurological Foundation and Eyes High Doctoral Scholarship and NSERC Brain Create to J.E.S.; Ambizione Fellowship to J.W.S., (PZOPP3\_208988) and subsidy to G.C. (310030\_185214 and 310030\_215668); European Research Council (ERC-2015-Cog HOW2WALKAGAIN 682999, and Marie Skłodowska-Curie individual fellowship 842578 to J.W.S.); the Swiss National Supercomputing Center; the Promobilia Foundation (to M.A.A.); the Swiss National Science Foundation (3200030-22828 to M.A.A.); Wings for Life (to M.A.A. and G.C.); Friedrich Flick Förderungsstiftung through Wings for Life (M.A.A. and G.C.), gifts from Bob Yant and Ann Kenowsky (to M.A.A.); and Wyss Center for Bio and Neuroengineering (to M.A.A.). We are grateful to B. Schneider and S. Arber for providing viral vectors, F. Merlos for the illustrations, and the Advanced Lightsheet Imaging Center at the Wyss Center for Bio and Neuroengineering. This work was supported in part using the resources and services of the Gene Expression Core Facility at the School of Life Sciences of EPFL.

**Author contributions** J.E.S., R.H., J.W.S., A.A.P. and G.C. conceptualized and designed the experiments. J.E.S., R.H., L.M., M.G., A.L., S. Ceto, C.K., T.H., M.T., S.A., M.A.A. and J.W.S. performed the rodent experiments. R.C., F.G., S. Casha, J.R., K.L.-K., N.H., A.G., R.D., L.A., A.A.P. and J.B. performed the human experiments. J.E.S., R.H., M.G., A.Y.Y.T., M.A.S., N.H., A.G., Q.B. and J.W.S. analysed the data. X.K., Y.V., E.M.-M., S.L., J.W.S., A.A.P. and G.C. designed the hardware and software for neurostimulation. J.E.S., R.H., J.W.S., A.A.P. and G.C. wrote the manuscript. All authors contributed to editing the manuscript.

**Competing interests** G.C., A.A.P., J.W.S., J.B., R.D. and S.L. hold various patents in relation to the present work. G.C., A.A.P. and R.D. are consultants of ONWARD Medical. G.C., A.A.P., J.W.S., J.B. and S.L. are minority shareholders of ONWARD, a company with direct relationships with the presented work. The other authors declare no competing interests.

**Additional information**

**Supplementary information** The online version contains supplementary material available at <https://doi.org/10.1038/s41586-025-09487-w>.

**Correspondence and requests for materials** should be addressed to Jordan W. Squair, Aaron A. Phillips or Grégoire Courtine.

**Peer review information** *Nature* thanks Jun-An Chen and the other, anonymous, reviewer(s) for their contribution to the peer review of this work.

**Reprints and permissions information** is available at <http://www.nature.com/reprints>.